NASA CONTRACTOR
REPORT

NASA CR-418

NASA CR-418

SHOCK TUBE DETERMINATION OF THE DRAG COEFFICIENT OF SMALL SPHERICAL PARTICLES

by Bruce P. Selberg

Prepared under Grant No. NsG-86/23-05-003 *by*
UNIVERSITY OF MICHIGAN
East Lansing, Mich.
for

NATIONAL AERONAUTICS AND SPACE ADMINISTRATION • WASHINGTON, D. C. • APRIL 1966

SHOCK TUBE DETERMINATION OF THE DRAG COEFFICIENT OF SMALL SPHERICAL PARTICLES

By Bruce P. Selberg

Prepared under Grant No. NsG-86/23-05-003 by
UNIVERSITY OF MICHIGAN
East Lansing, Mich.

for

NATIONAL AERONAUTICS AND SPACE ADMINISTRATION

For sale by the Clearinghouse for Federal Scientific and Technical Information
Springfield, Virginia 22151 – Price $1.50

ACKNOWLEDGEMENTS

This investigation was supported by the National Aeronautics and Space Administration in the form of a grant, NsG-86-60. The author wishes to thank Professors J.A. Nicholls and Martin Sichel for their helpful suggestions and criticisms. Special appreciation is given to Professor J.A. Nicholls and Stuart W. Bowen for their advice, discussions, and encouragement throughout the study.

Further appreciation is extended to Philip Malte who wrote the computer programs and helped with experiments, to Cletus Iott who provided assistance with the electronic instrumentation and the optical system, to Pai-Lien Lu who took the photomicrographs, and to other members of the Aircraft Propulsion Laboratory who contributed in various ways to this work.

TABLE OF CONTENTS

TABLE OF CONTENTS (cont)

LIST OF TABLES

LIST OF FIGURES

LIST OF FIGURES (cont)

NOMENCLATURE

A	Projected characteristic area based on particle diameter
A_c	Acceleration modulus ($\alpha d/U_R^2$)
Atm	Atmosphere
a	Speed of sound
C_D	Drag coefficient ($F_D/1/2\,\rho\,U_R^2\,A$)
C_f	Skin friction coefficient
d	Sphere diameter
F	Force vector
g	Acceleration due to gravity
Hg	Mercury
I_{sp}	Specific impulse
m	Mass
M	Mach number
M_R	Relative Mach number (U_R/a)
$\cancel{M}$	Camera magnification
P	Pressure
PV	Evacuated pressure ($P_{atm} - P_1$)
Re	Reynolds number ($\rho U_R d/\mu$)
T	Temperature
t	Time

NOMENCLATURE (cont)

τ	Non-dimensional time
u	Axial velocity
U_2	Convective flow velocity
U_R	Relative velocity ($U_R = U_2 - V_p$)
U_s	Sphere rotation speed
V_p	Particle velocity with respect to inertial space
x	Displacement of particle
α	Particle acceleration with respect to inertial space
δ	Boundary layer thickness
δ^*	Displacement thickness
ρ	Density
μ	Viscosity
$\bar{\mu}$	Microns
ν	Kinematic viscosity ($\nu = \mu/\rho$)
ϕ	Axial velocity ratio (u_p/u_g)
$\frac{\sqrt{\overline{U'^2}}}{U}$	Relative turbulent intensity

SUBSCRIPTS

g	Gas conditions
m	Microsecond timer

NOMENCLATURE (cont)

SUBSCRIPTS (cont)

p	Particle conditions
R	Relative conditions
w	Wake conditions
1	Initial conditions at test section
2	Convective flow conditions

ABSTRACT

An experimental study was conducted to determine the drag coefficient of inert spherical particles accelerating in a laminar, non-reacting, incompressible continuum flow. The Reynolds number range which was covered in the study was from 150 to 1700, and particle sizes ranged from 150 $\overline{\mu}$ to 450 $\overline{\mu}$.

The convective flow behind the shock wave in a shock tube was used to accelerate the particles. The particle's diameter and the displacement versus time measurements were obtained using a rotating drum camera in conjunction with an oscillating light source. The photographic data, the particle density, the shock speed, and the initial pressure and temperature in conjunction with the normal shock relations were combined to calculate the drag coefficient.

The drag coefficient is usually considered to be a function only of Reynolds number and acceleration modulus, however, C_D varies considerably because of particle roughness. Experiments with HP 295 ball powder, whose surface is relatively rough, produced results which were as much as 85 per cent higher than the steady state curve, with the increase dependent upon the relative Mach number of the flow about the particle. Similar drag coefficient experiments with smooth sapphire balls did not produce the scatter, the higher values, nor the dependence on relative Mach number.

I. INTRODUCTION

1.1 ORIGIN OF THE PROBLEM

In order to improve the density and specific impulse characteristics of solid propellant rocket fuels, small metal particles are mixed into the propellant. During combustion, condensed liquid and solid metal oxide particles are formed from the combustion products. These particles comprise 30-40 per cent by weight of the combustion products in current solid propellant rocket motors. Because of inertia effects, these particles leave the nozzle at lower velocity which means a loss of momentum and hence a loss in specific impulse. In order to calculate the loss in specific impulse due to the velocity and temperature lags, the drag coefficient of the particles is one of the variables which must be known.

Presently most of the specific impulse loss calculations are made using the "standard drag coefficient curve" for spheres. This curve is only valid for a single smooth sphere in a steady, incompressible, laminar, non-reacting, and continuum flow field, conditions which are certainly not satisfied in a rocket nozzle. Thus, in a rocket engine a particle is moving in an accelerating, turbulent, compressible stream whose temperature is different than that of the particle. The particle also moves from the continuum regime to the slip flow regime and possibly to the free molecule regime depending on its size and the flow in the rocket nozzle. Figure 1

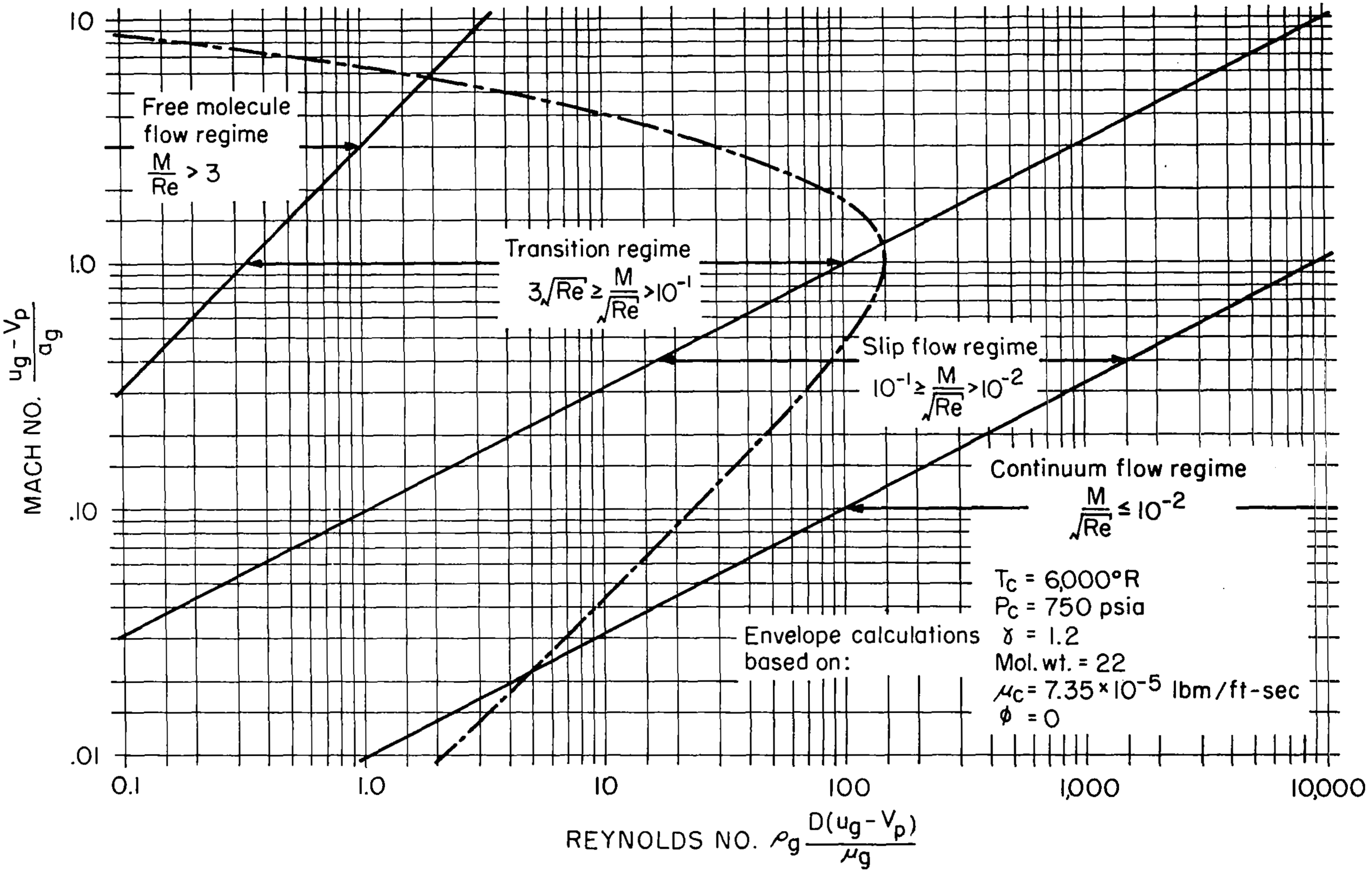

Figure 1. Mach Number—Reynolds Number Flow Regimes Encountered by a Five-Micron Particle in a Rocket Nozzle

represents the path in the Mach number Reynolds number regime which a five-micron particle, produced under chamber conditions typical of solid propellant rocket motors, can experience(1). In some cases enough particles are present such that the particles and the gas must be analyzed as a two-phase flow. The particles may remain hot enough, due to the temperature lag, to emit electrons by means of thermionic emission or to change the drag due to heat transfer. Some of the particles which come through the nozzle are the original metal particles which are mixed into the propellant. The drag coefficient of these particles will be a function of all the above effects plus burning.

In order then to determine the correct drag force on a particle in a solid rocket motor nozzle, the influence of all of the above parameters must be studied.

1.2 REVIEW OF STUDIES ON THE DRAG COEFFICIENT OF PARTICLES

Some theoretical and experimental work has been done to determine the drag coefficients of particles accelerating in the incompressible continuum flow regime. The results of these studies differ appreciably from one another as may be seen in Fig. 2.

Ingebo(2) conducted experimental studies on the vaporization rates and drag coefficients for isotane sprays accelerating in turbulent air streams. He injected the liquid drops into air streams moving at 140

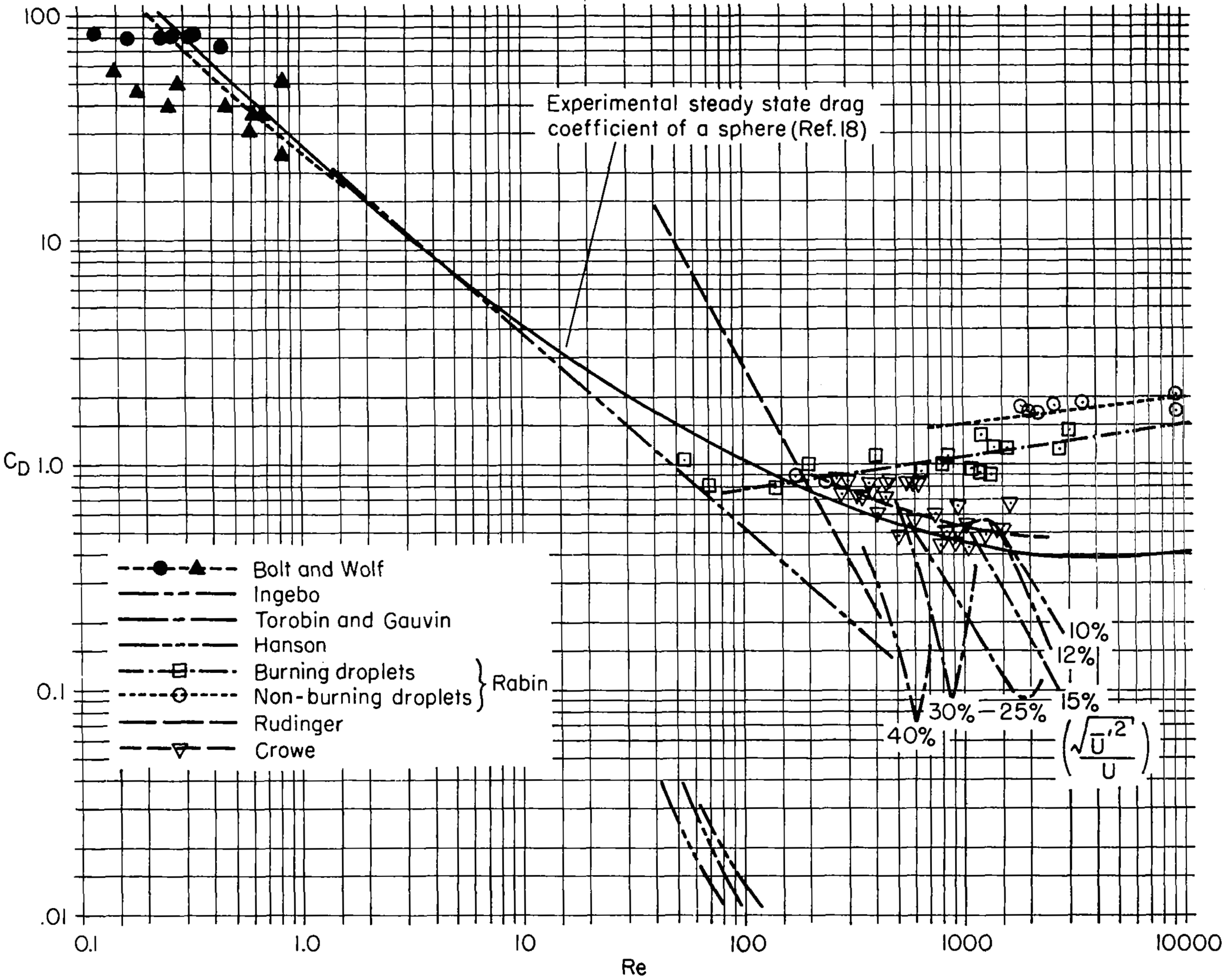

Figure 2. Data on the Drag Coefficient of Spheres

and 180 ft/sec. A specially designed camera was used to obtain drop-size distributions and drop-velocity data. He was then able to obtain vaporization rates and drag coefficients for the liquid drops. He found his results could be represented by a single curve given by

$$C_D = \frac{27}{Re^{.84}}$$

Fledderman and Hanson$^{(3)}$ performed similar experiments by photographing spray droplets accelerating in streams moving from 50 to 75 ft/sec. Their results are one hundredth the steady state value for a sphere.

Experimental drag coefficient studies of burning kerosene drops have been done by Bolt and Wolf$^{(4)}$ for $Re < 1$. These results indicate a decrease in the drag coefficient due to burning.

Rabin et al.$^{(5)}$ determined the drag coefficient of burning and non-burning liquid fuel droplets accelerating due to the convective flow behind a shock wave. For $Re > 200$ Rabin's drag coefficients were greater than those of a sphere in steady flow. Rabin's data also indicates a decrease in drag coefficient due to burning.

Rudinger$^{(6)}$ also used the convective flow behind a shock wave to determine the drag coefficient of accelerating glass beads, which had an average diameter of 29 microns. The x versus t motion was recorded by streak photography. The Reynolds number range of the experiment was from 40 to 300. Rudinger found that all his data could be correlated by the expression

$$C_D = \frac{6000}{Re^{1.7}}$$

This relationship deviates widely from the steady state curve for spheres and Rudinger suspects that electric charges on the particles may be the cause of the deviation.

A very thorough literature survey on "The Fundamental Aspects of Solids-Gas Flow" was made by Torobin and Gauvin(7-12). They listed and discussed such problems as the sphere wake in laminar fluids; accelerated motion of a particle in a fluid; the effects of particle rotation; roughness and shape; and the effect of fluid turbulence on the particle drag coefficient. They also made an experimental study of the drag coefficients of single spheres moving in steady and accelerated motion in a turbulent fluid. Small radioactive smooth spheres were fired into a turbulent flow wind tunnel of known turbulence intensity and the motion of the sphere was recorded by means of a radioactive sensing device. Using this technique, continuous x versus t data could be obtained for the spheres. It was found that by increasing the turbulent intensity level, the critical Reynolds number could be shifted to Reynolds numbers as low as 400 and that drag coefficient was independent of acceleration in turbulent flow.

Recently Crowe(13) did both an analytical and experimental study to determine the effects of burning, evaporation, and acceleration on the drag coefficients of particles accelerating in gas streams. The Reynolds number range extended from 250 to 1600. Both the analytical and experimental portions of the study were confined to the incompressible continuum flow regime.

For the analytical study Crowe chose a spherical model with mass flux through the surface to simulate burning and evaporation. The tangential equation of motion was used as the governing equation in the analysis of the boundary layer flow about the sphere. The velocity distribution outside the boundary layer was assumed to be that corresponding to inviscid flow. With the proper boundary conditions,the equations were solved indicating that for burning or evaporating particles the skin friction coefficient is reduced. A constant form drag coefficient was assumed and used for all the results. The total drag coefficient is then just the sum of the skin friction and form drag coefficients.

For the experimental portion of his study, Crowe used the convective flow behind a shock wave to accelerate the particles. A high speed framing camera was used to record the particle diameters and x versus t history. With the shock speed, the particle density, and the local temperature and pressure known, Crowe was able to calculate the drag coefficient. Crowe's particle size varied from 100 to 350 microns.

Crowe's best fit curve to his experimental non-burning data is approximately 15 per cent higher than the steady drag coefficient curve. His analytical results are another 15 per cent above his experimental data. However, each experimental point has approximately a 40 per cent probable error.

1.3 PURPOSE OF THIS STUDY

The present study is part of an overall investigation to study the dynamics of inert, reacting, and charged particles in solid rocket motor nozzles, and is a continuation of Crowe's work. Basically it is desired to experimentally determine the relation between C_D and the prime variables Re, $M_R/\sqrt{Re}$, M_R, and a non-dimensional burning rate parameter. In addition the effect of the secondary variables, relative turbulent intensity, unsteady effects in the particles wake, particle rotation, and particle roughness are also to be studied.

Due to the relatively large experimental error and scatter in Crowe's data which would obscure slip and compressibility effects, it was necessary to repeat the incompressible continuum flow regime before conducting experiments in the slip flow regime with compressibility effects. In order to determine C_D more accurately, a new and better instrumented shock tube was constructed. This study is primarily concerned with a more accurate determination of the drag coefficient of small spherical particles accelerating in the incompressible continuum regime.

II. PARTICLE EQUATIONS OF MOTION

Newton's second law of motion states that the rate of change of momentum of a particle is equal to the sum of the forces which act on the particle and is in the direction in which the sum of the forces acts. In mathematical form Newton's law is

$$\sum \vec{F} = m \vec{\alpha} \tag{1}$$

The forces are the viscous and pressure forces which act on the particle surface and the body forces which act on the particle mass. If the pressure and viscous forces are expressed in terms of a drag coefficient, then Eq. (1) can be written as

$$C_D \frac{\rho}{2} \left| \vec{U}_R \right| \vec{U}_R A + m\vec{f} = m \vec{\alpha} \tag{2}$$

where C_D = drag coefficient of the particle

α = acceleration of the particle with respect to inertial space

ρ = density of the fluid

U_R = relative velocity between the particle and the fluid

A = projected characteristic area based on particle diameter

m = mass of particle

f = body force per unit mass.

For the case of burning particles Eq. (2) would contain an additional term for the momentum flux from the particle's surface. The body force term in this analysis is the gravitational force term that acts on the body. In the present study the particle is accelerated by the convective flow behind a shock wave so that the acceleration due to the viscous and pressure forces is much greater than that due to gravity, i.e.,

$$\frac{\alpha_v}{g} \geq 100$$

Thus the gravitational force term will be neglected. Equation (2) may be written as

$$C_D \frac{\rho}{2} |\vec{U}_R| \vec{U}_R A = m\vec{\alpha} \tag{3}$$

Since the flow velocity and the acceleration vector are in the same direction, the vector notation may be dropped and Eq. (3) becomes

$$C_D = \frac{2m\alpha}{\rho U_R^2 A} \tag{4}$$

For spherical particles of uniform density,

$$C_D = \frac{4\rho_p \alpha d}{3\rho U_R^2} \tag{5}$$

where ρ_p = particle density

d = particle diameter.

Dimensional analysis indicates that the other similarity parameters which are needed to properly determine the drag coefficient of a non-burning smooth spherical particle in a laminar flow field subject to compressibility and non-continuum effects are Reynolds number, Re, Mach number, M_R, $M_R/\sqrt{Re}$, and acceleration modulus, A_c. In terms of the present notation Reynolds number and Mach number are

$$Re = \frac{\rho U_R d}{\mu} \tag{6}$$

$$M_R = \frac{U_R}{a} \tag{7}$$

The particle flow regime is determined by the value of $M_R/\sqrt{Re}$. The different flow regimes are defined as follows(14):

$$\frac{M_R}{\sqrt{Re}} \leq 10^{-2} \qquad \text{continuum regime}$$

$$10^{-2} < \frac{M_R}{\sqrt{Re}} \leq 10^{-1} \qquad \text{slip flow regime}$$

$$10^{-1} < \frac{M_R}{\sqrt{Re}} \leq 3\sqrt{Re} \qquad \text{transition regime}$$

$$\frac{M_R}{Re} > 3 \qquad \text{free molecular flow regime}$$

As seen in Fig. 1, a five-micron particle in a typical solid propellent rocket nozzle experiences all of the above flow regimes as it travels through the nozzle. Equations (5) and (6), along with experimental data, can be used to calculate the C_D and Re of a non-reacting spherical particle. Although this report is concerned only with the incompressible continuum regime, the calculation of M_R, and $M_R/\sqrt{Re}$ are needed to insure that the particle is in the desired flow regime.

III. EXPERIMENTAL APPARATUS

3.1 CHOICE OF EXPERIMENTAL FACILITY

In order to study the dynamics of solid particles in rocket nozzles, an experimental facility must be able to produce a particle environment under which the following parameters can be studied:

1. Acceleration modulus
2. Mach number
3. Mach number/ $\sqrt{\text{Reynolds number}}$
4. Burning rate parameter
5. Electric charges on particles

A shock tube was chosen because by using the convective flow behind the shock front in connection with the small spherical particles (50-500 microns in diameter), it is possible to produce the flow conditions under which the above parameters can be studied. This type of facility was used successfully by both Crowe(13) in studying the drag coefficient of solid particles and by Rabin(5) in studying the shattering of liquid drops.

3.2 DESCRIPTION OF FACILITY

The experimental equipment consists of a horizontal shock tube into which the particles are injected and then accelerated by the convective flow field behind the shock front. The distance, x, versus time, t, of the particles is recorded by a modified AVCO rotating drum camera in conjunction with a high voltage switching circuit which supplies energy to a Xenon flash tube. By combining the x versus t data, the shock strength, and the initial conditions, the drag coefficient of the particle can be obtained.

3.2-1 Shock Tube and Driver Section

The 1 3/8 inch square shock tube consists of a three foot stainless steel driver, a six foot stainless section between the driver and the test section, a one and one-half foot aluminum test section, and a six foot stainless section downstream of the test section.

The diaphragm material is ruptured by means of a long rod which is inside the driver section and is driven by a Saval 24 volt D. C. solenoid. A photograph of the driver section appears in Fig. 3. Two different types of material have been used as diaphragms for the weakest shock waves. First, Dupont 220 MD-31 cellophane was used. This material tended to shatter into small pieces which necessitated frequent swabbing of the shock tube. The second type diaphragm material that was used was Dupont mylar, .0015 inches thick. The mylar was a tougher material and was used for the stronger shock runs. Unlike the cellophane, the mylar did not shatter when punctured but just folded back. However, more energy was lost in this folding process and it took a higher driver pressure using mylar to achieve the same shock Mach number than it did when cellophane was used.

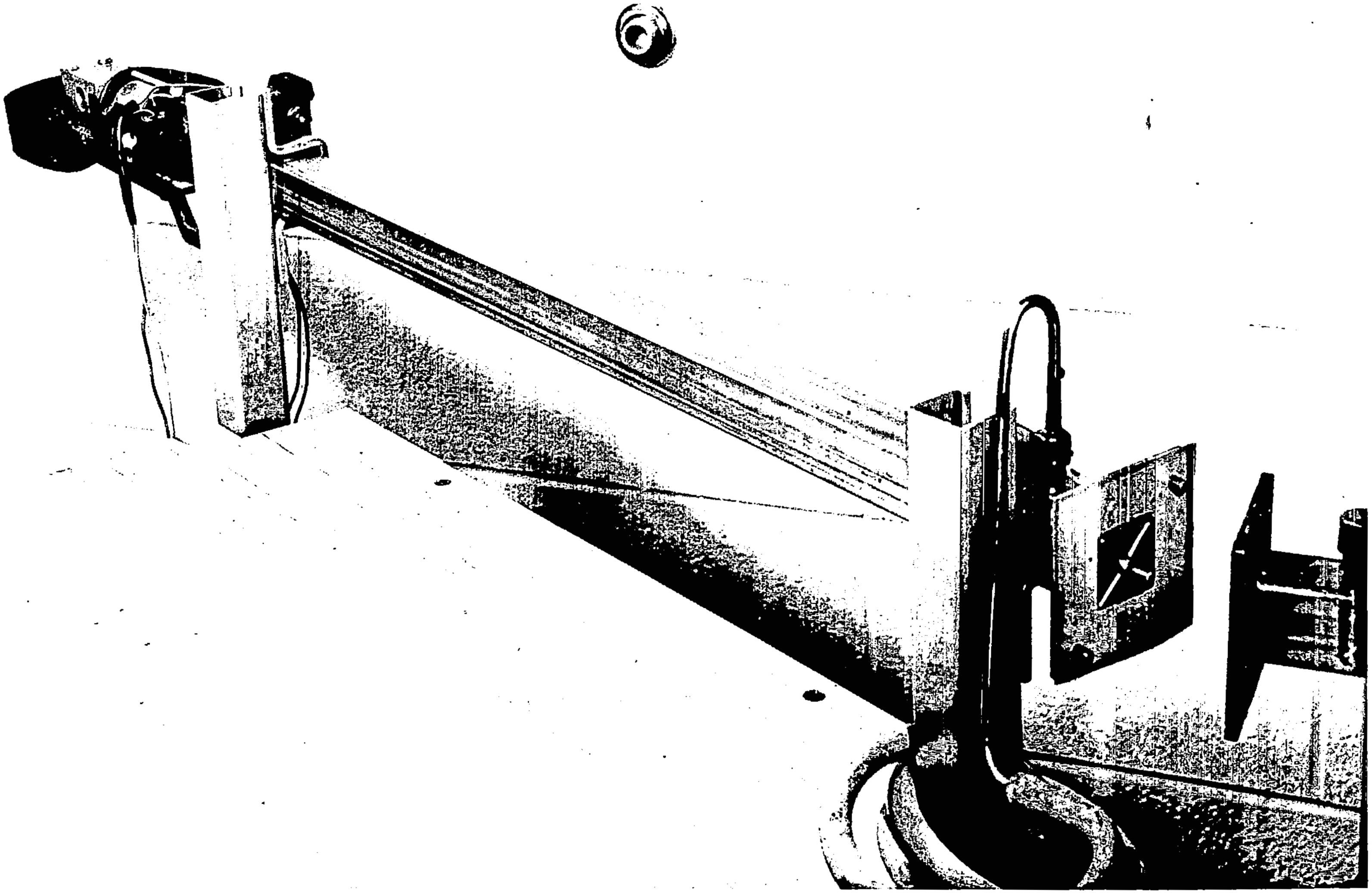

Figure 3. Shock Tube Driver Section

3.2-2 Optical Equipment

The test section windows, through which the x versus t history of the particles is recorded, are 1 1/2 inches high and 4 inches long of optically-flat glass.

A modified AVCO rotating drum camera is used in conjunction with an oscillating light source to take shadowgraph pictures of the particle's trajectory. The physical layout of the optical system is reproduced in Fig. 4.

The drum camera is mounted on a lathe bed with two compound rests, with rotating drum and main camera body on one compound rest and the camera lens mounted on the other. A flexible bellows connects the lens and the camera body. This arrangement permits accurate and independent movement of the lens and body both perpendicular and parallel to the test section. Thus the magnification can be changed as desired and the length of the test section can be traversed with the lathe setup. The lens is a Goerz Red Dot Artar process lens, which is a highly corrected lens designed for applications where the image to film distance and the object to film distance are of the same order.

The light source is a PEK XE-9 Xenon flash tube. The energy is switched to the Xenon tube via a modified version of a Edgerton, Germeshausen, and Grier LS-10 multiple microflash system. This system

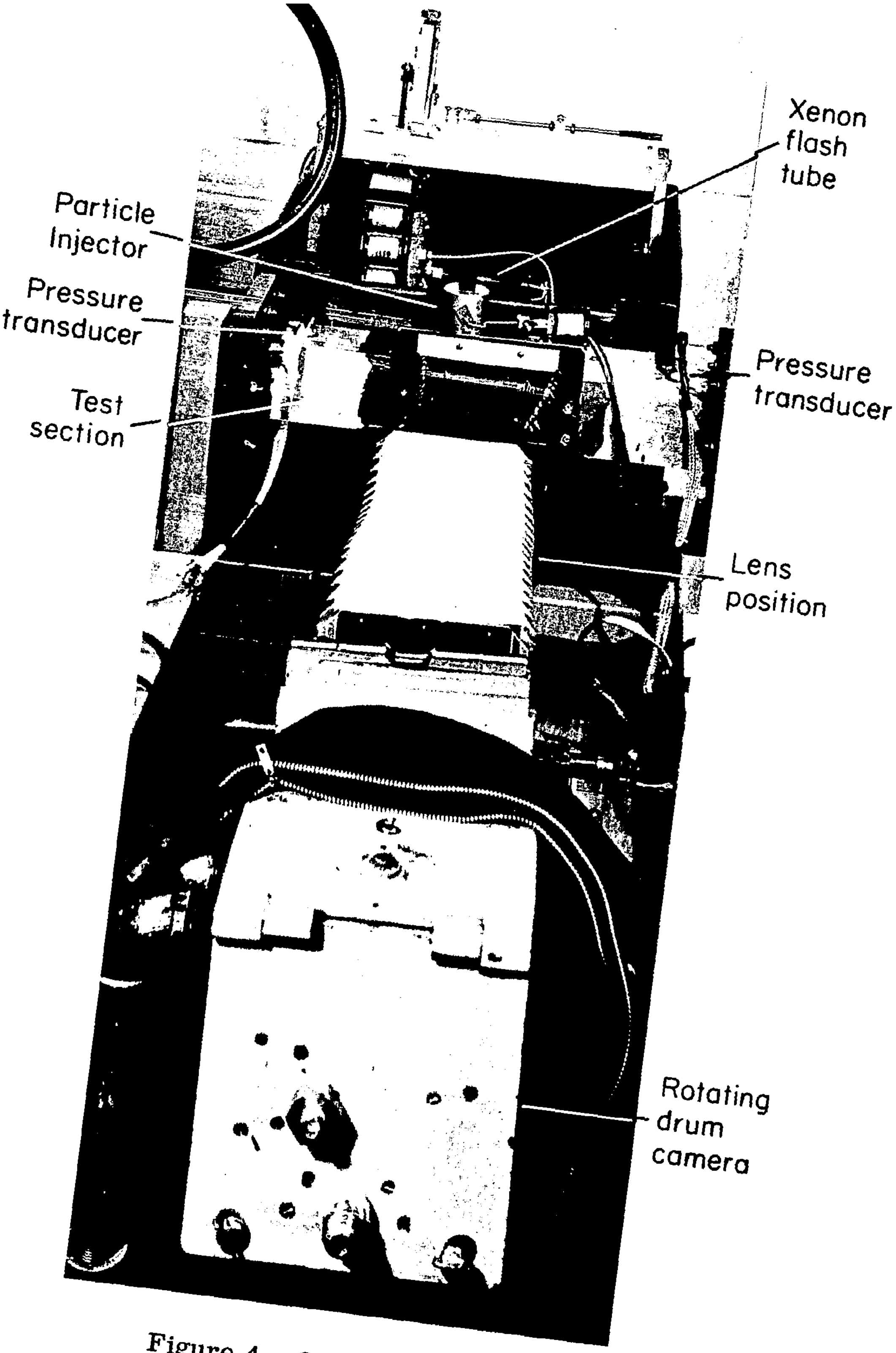

Figure 4. Optical System

includes a low voltage power supply, a pulse shaper unit, a time delay unit, and five high voltage discharge units. The switching circuits control the discharge to the Xenon flash tube of one .001 microfarad capacitor bank and four .005 microfarad capacitor banks, all charged to 12 kilovolts. The switching circuit is activated by a signal generator pulse-shaper unit. By varying the frequency of the signal generator, it is possible to vary the time interval between flashes from 10 milliseconds to 10 microseconds. A schematic diagram of the modified EG and G unit is in Fig. 5.

To achieve the shortest possible rise time, it is necessary to reduce the circuit inductance to a minimum since the resistance of the ionized Xenon gas is only 2 Ω. This was accomplished by modifying the high voltage discharge units of the multiple microflash system. The high voltage section of the first switching unit was installed as close to the Xenon tube as possible as is in Fig. 6. A spark gap is used in the first unit as the switch for the energy. This was done since the spark gap will switch the current faster than the mercury diode of the other four units. With the above arrangement it was possible to obtain a 480 nanosecond width for the light pulse to decay to 10 per cent of its peak value.

The Xenon flash lamp is mounted on a drill press milling vise, permitting motion both perpendicularly and parallel to the test section. Both collimated and quasi-collimated light have been used in the system.

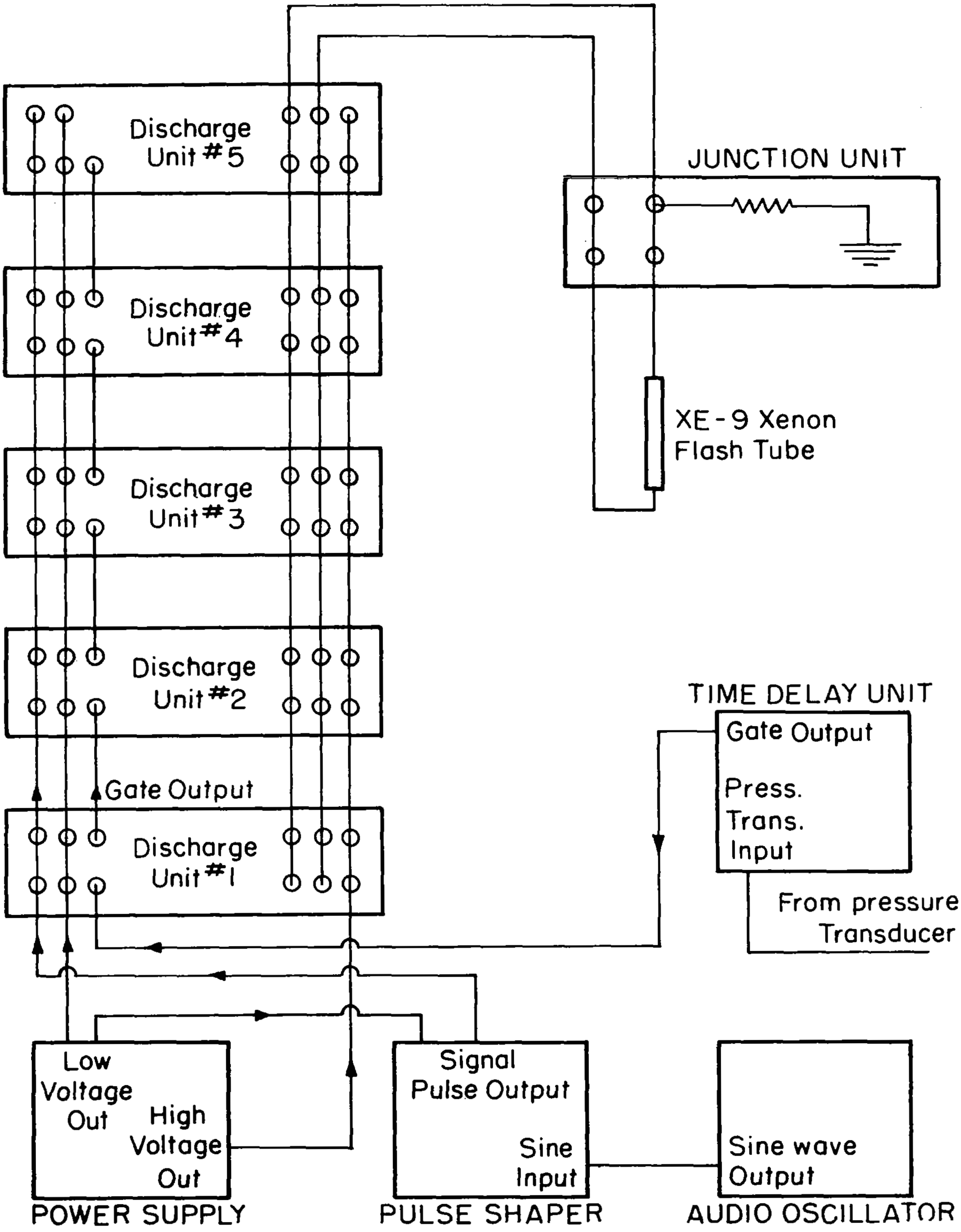

Figure 5. Schematic Diagram of Microflash System

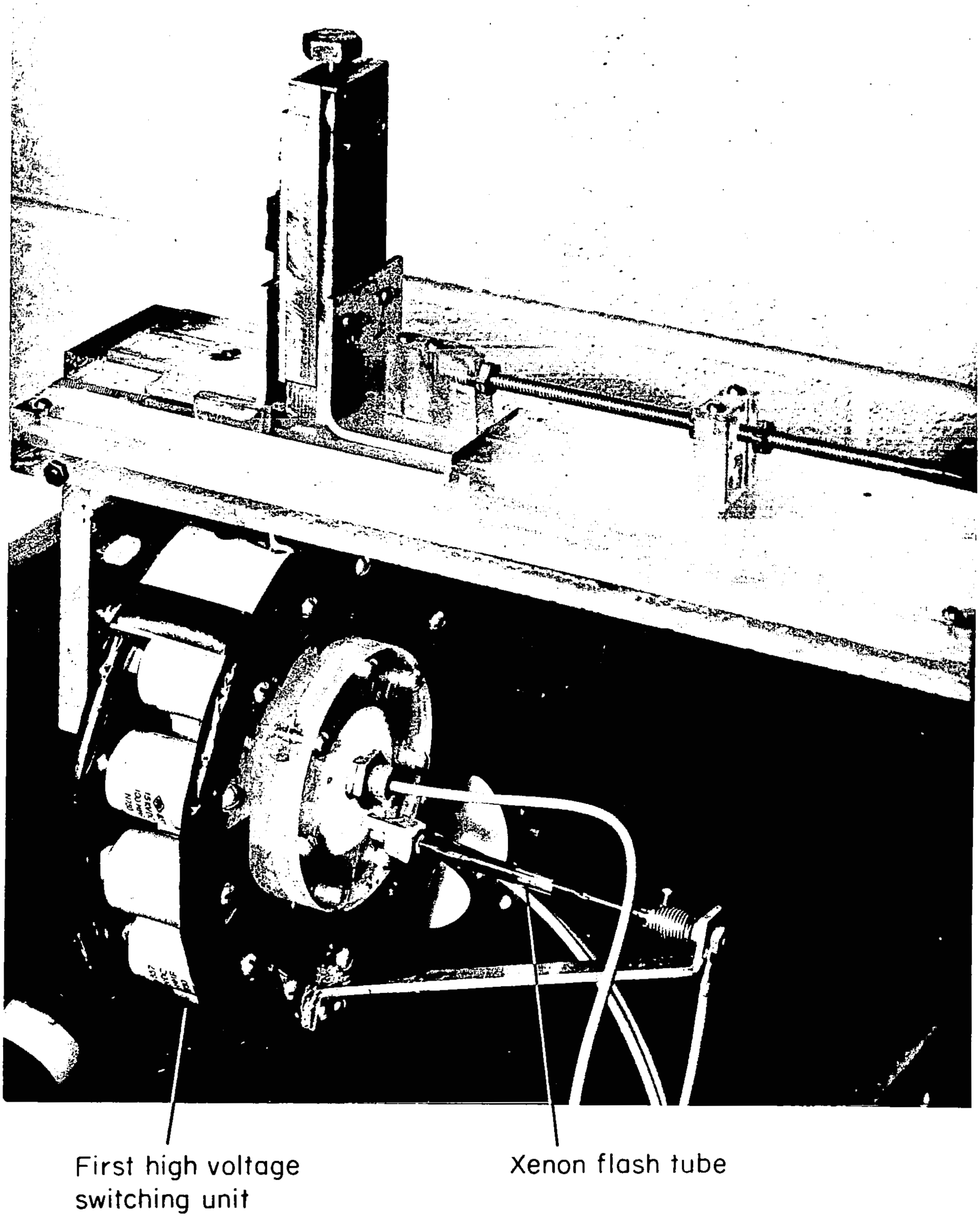

Figure 6. First Switching Unit and Zenon Flash Tube

Two types of film have been used in the experiment: Kodak Royal Pan and Kodak Plus X film.

3.2-3 Particle Injector System

Within the particle injector, shown in Fig. 7, the particles are placed on a circular platform which is rotated on its axis by means of a solenoid thus injecting the particles into the test section. The particle injector is designed so that its pressure is the same as that in the test section and the hole in the test section is .059 inches in diameter.

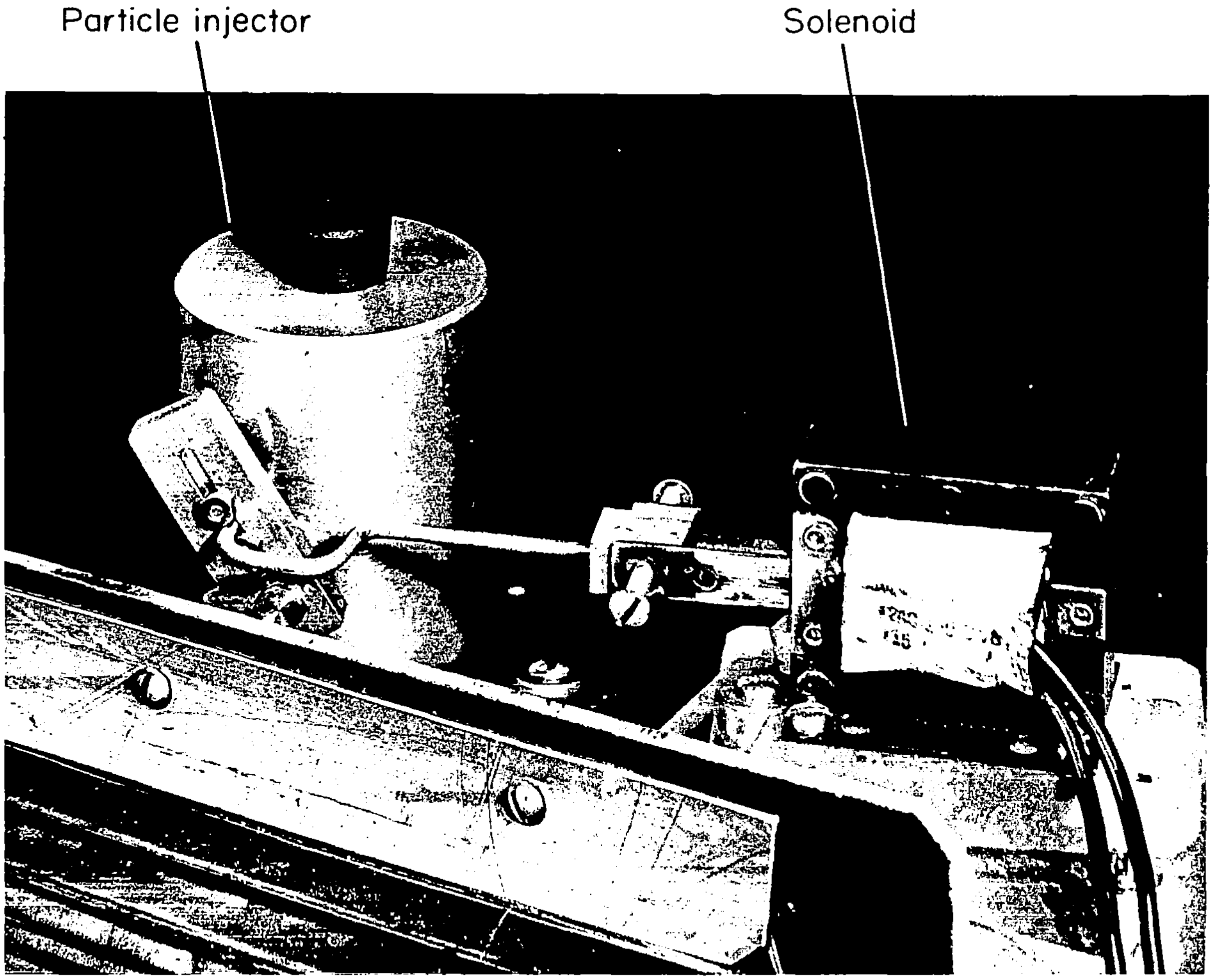

Figure 7. Particle Injector

3.2-4 Shock Speed Measurement

The shock speed is measured with two flush-mounted Kistler model 701A quartz pressure transducers, 1.1667 feet apart, in conjunction with a microsecond timer. The transducers have a rise time of ten microseconds. Two Kistler model 566 multi-range electrostatic charge amplifiers are used to amplify the signals from the transducers. These signals are in turn fed to the start and stop channels of a Transistor Specialties Incorporated microsecond Timer. The above transducers are very sensitive and thus allow the recording of very weak shock waves. Desiring the best possible measurement of the wave speed, the transducers were mounted equally upstream and downstream of the test section.

3.2-5 Pressurization and Vacuum System

A schematic diagram of the pressurization and vacuum system is shown in Fig. 8. The system was designed so that the shock tube and driver section could both be evacuated to any desired pressure. The valve arrangement is such that the initial pressure can be controlled in the driver section and shock tube independently. In a similar fashion both the driver section and the shock tube can be pressurized in an independent controlled fashion. With this flexibility it is possible to maintain certain desired shock strengths while varying the Re number and $M_R/\sqrt{Re}$.

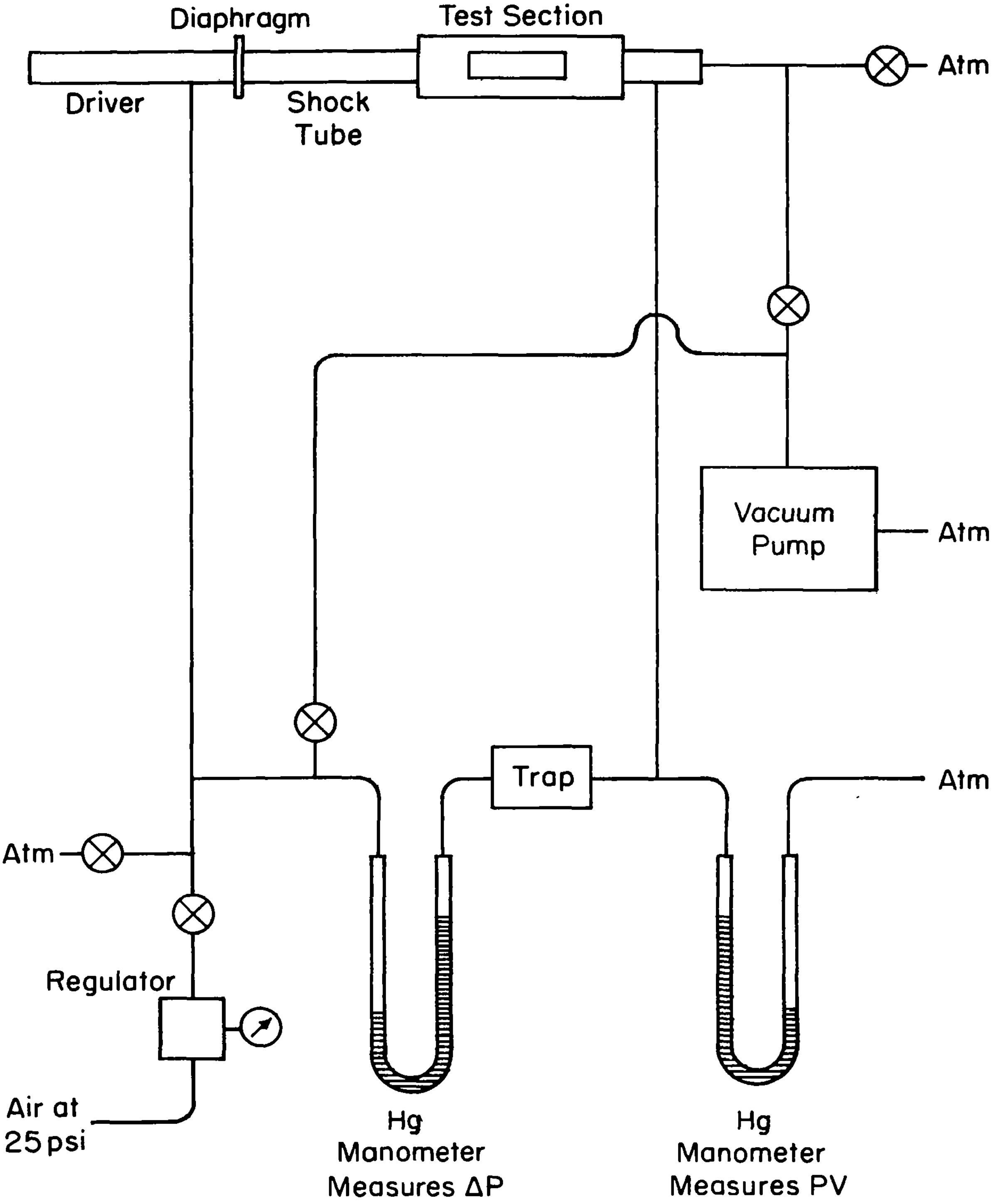

Figure 8. Schematic Diagram of the Pressurization and Vacuum System

3.2-6 Sequential Timing During Experiment

To have the particles in correct position and to begin the photographing sequence at that time, an accurate timing sequence is necessary. Figure 9 is a schematic diagram of this sequencing system. Once the particles are dropped, there must be an accurate delay before the solenoidal drive rod punctures the driver diaphragm. This is accomplished by means of a thyratron time delay unit. A circuit diagram of this circuit appears in Fig. 10. A second sequencing unit is needed to start the photographic process. This is accomplished by having the signal from the first pressure transducer sent to a second time delay unit which, after a sufficient delay allowing time for the shock to travel to and interact with the particles, sends another signal to the first high voltage switching circuit. The high voltage switching circuit then dumps its energy into the XE-9 flash tube and the picture-taking sequence is begun. Figure 11 is a view of the overall facility.

3.2-7 Experimental Procedure

The normal experimental procedure is as follows:

1. Load camera
2. Record atmospheric pressure
3. Record atmospheric temperature
4. Install diaphragm

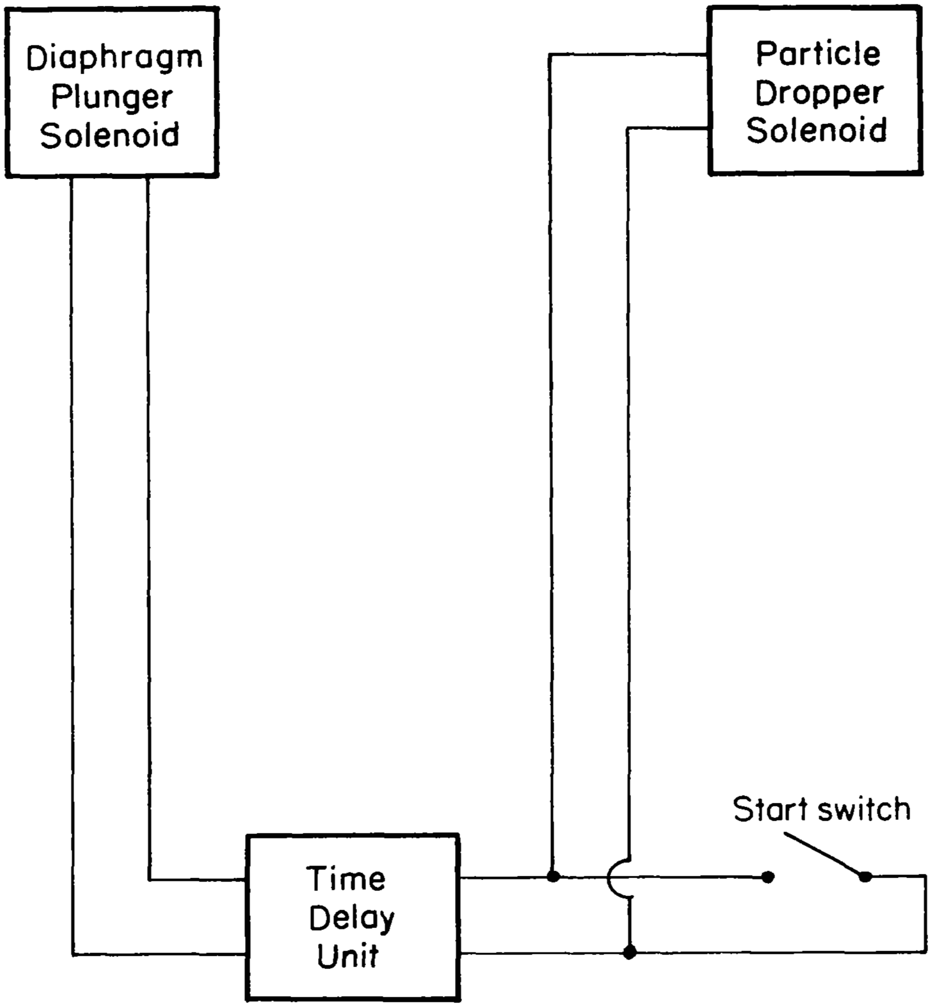

Figure 9. Schematic Diagram of Time Delay Sequencing System

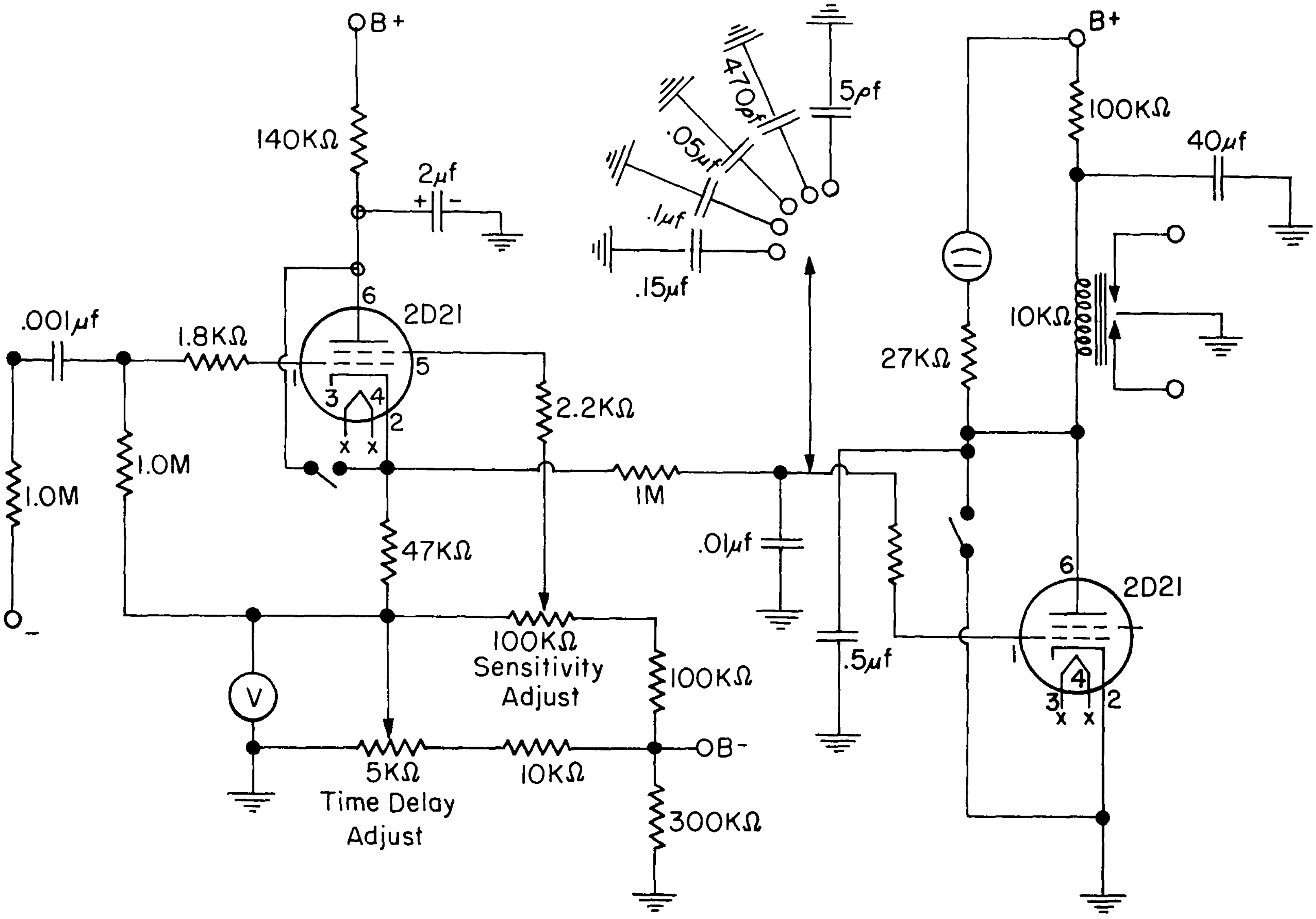

Figure 10. Circuit Diagram of Time Delay Unit

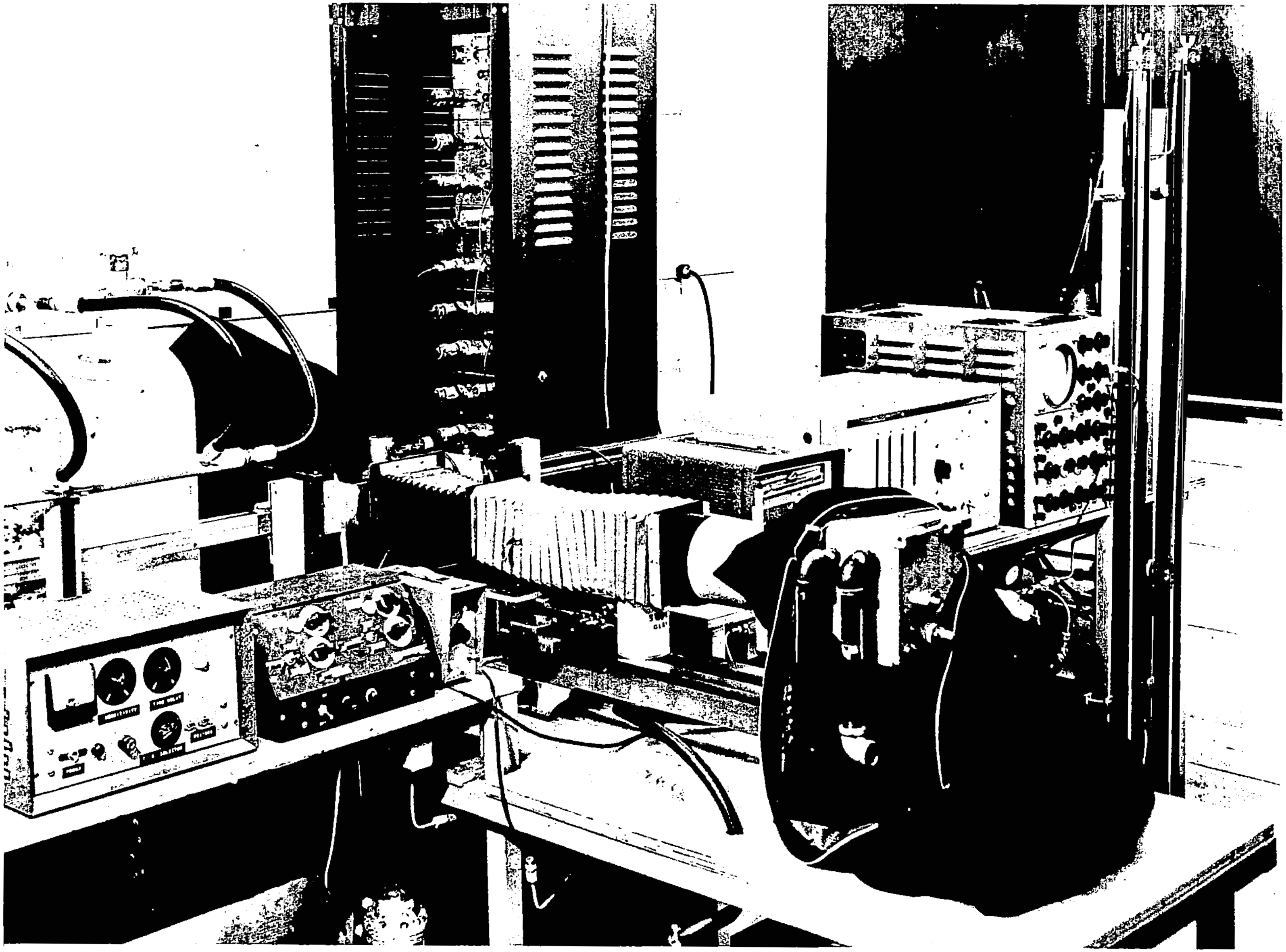

Figure 11. General Shock Tube Facility

5. Load injector
6. Evacuate, pressurize, or both
7. Adjust sensitivity levels
8. Read test section pressure
9. Run rotating drum camera up to speed
10. Engage start switch
11. Record microsecond timer reading
12. Mark and remove film from camera
13. Develop film.

3.3 CALIBRATION OF EQUIPMENT

All of the parameters except ρ_p which are needed to calculate C_D are obtained from data that is recorded during an experiment. Thus it is essential that the experimental equipment has been properly calibrated, and this calibration procedure is described below.

3.3-1 Shock Velocity Measurement

The convective flow velocity, U_2, and the gas density in the convective flow region, ρ_2, are obtained from the measurements of shock velocity, C_s, initial temperature, and initial pressure and application of the normal shock relations. For weak shock waves U_2 is very sensitive to changes in C_s, or the time for the shock wave to travel the distance between the two pressure pickups. This time measurement must therefore be very accurate.

The linearity and slope of the signals from the pressure transducers were checked by putting the output from the amplifiers of the transducers into a Tektronix oscilloscope and photographing the trace with a Polaroid attachment. Photographs of the traces were taken of the start transducer and its amplifier and of the stop transducer and its amplifier at equal shock strengths. The amplifiers were then interchanged and the procedure was repeated at the same shock strengths. Upon comparing the results it was found that the four traces are virtually indistinquishable. Two pictures of such traces appear in Fig. 12a and 12b.

The sensitivity adjustments on the start and stop channels of the microsecond timer were calibrated so that both channels could be set at the same level. The gain on the amplifier and the sensitivity on the microsecond timer were always adjusted so that both channels of the timer would be activated on about the first 10 per cent of the signal from the pressure transducers.

Since the slopes and linearity of the two transducer amplifier combinations were the same and the sensitivities on the timer were adjusted to the same level, the shock speed that was measured by the transducer microsecond timer combination would be the actual shock speed if shock

Start transducer

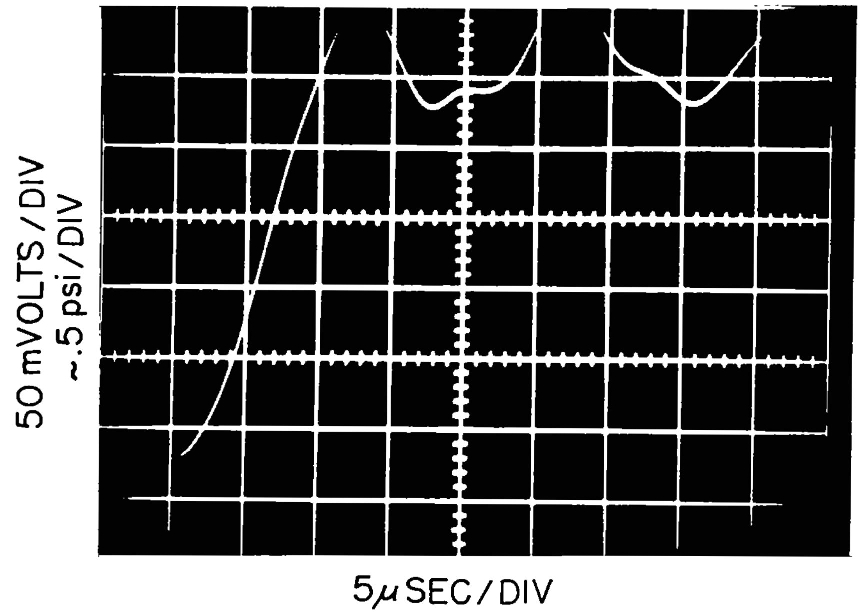

Stop transducer

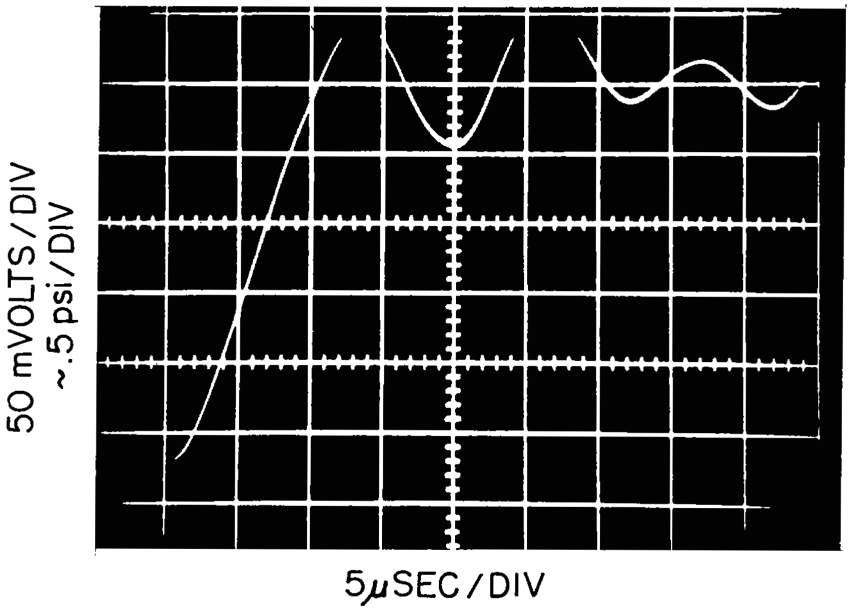

Figure 12. Pressure Transducer Outputs

speed decay was unimportant. By setting the same driver to test section pressure ratio and making a series of shock runs, the time interval read on the microsecond timer would consistently be within plus or minus one microsecond out of 900 microseconds.

3.3-2 Schlieren Photographs of Shock Front

A Schlieren system was set up to verify the existence of a plane shock front and to make sure that the injector hole did not cause the front to bend locally. A spark gap triggered by the first unit of the multi-microflash was used as the light source for the Schlieren system. By incorporating the spark gap with the microflash system and varying the time delay in the microflash system, it was possible to take photographs of the shock front at various locations along the viewing area of the test section. In all cases the shock front was plane and perpendicular to the direction of flow. The fact that the shock front is plane and is perpendicular to the flow direction is justification for using the normal shock-tube relationships.

3.3-3 Calibration of Optical Equipment

The calibration of the optical equipment is extremely important for both the particle diameter, and the distance versus time data are obtained photographically. The camera was focused and the magnification was determined in the following way. A cylindrical rod, .043 inches in diameter, was inserted through the particle injector hole parallel to the test section walls. The rotating drum camera was then focused on the rod, and a picture of the rod was taken with the drum stationary. The film was developed and the negative was then viewed through a Bausch and Lomb microscope with graduated eyepiece to determine the size of the image. The magnification of the microscope had previously been determined using the grid from an Edmund comparator. Thus the magnification of the camera was known. Some doubt remained as to whether this magnification was correct in that the calibration probe was six times larger in diameter than the spherical particles and the test object was not spherical like the particles. Accordingly, synthetic sapphire spheres, .015 inches in diameter (± .0001 inches), were dropped through the particle injector and photographed. The photographic images of the sapphire balls yielded sphere diameters which were within .1 per cent of the actual sapphire sphere diameter. Thus, the method for determining the magnification factor proved acceptable.

Another optical test was made to determine whether the lines on a grid pattern remained straight and undistorted so that the particle displacement measurements would be true. A grid network on a clear plastic was inserted into the test section and photographed. By viewing the resulting image on the film no distortion could be detected. Thus the displacement measurements on the film would be a true representation of the actual movement of the particle.

To determine the influence of development time on image size, a final optical test was made. Three wires, 0.0036 inches, 0.0070 inches, and 0.0104 inches in diameter, were photographed nine times under the same conditions. Using Kodak D-11 developer at 68°F, each piece of exposed film was developed at times ranging from five to nine minutes at half-minute invervals—seven minutes being normal. Upon microscopic examination, no apparent diameter change could be detected in any of the three wires. Thus in actual experimental runs, it was determined that the development time could be varied plus and minus one minute without affecting the validity of the experimental results.

3.3-4 Shock Tube Attenuation

Ideally a shock wave propagates at a constant velocity in a shock tube. In actuality, however, the shock wave attenuates. The amount of this attenuation depends on several things: the strength of the original wave at the diaphragm, the distance of the measuring device from the diaphragm, and the size of the shock tube. An experimental study of attenuation in shock tubes was conducted by R. J. Emrich and C. W. Curtis(15). They conducted their experiments in shock tubes of various sizes. For a shock tube with the same hydraulic radius as in the present study, they found the following relationship to be valid within a factor of two.

$$\frac{dM}{dx} \simeq 5.08 \times 10^{-4} \frac{M^2 - 1}{M}$$

The shock Mach number was always less than 1.25. For M = 1.25 dM/dx is

$$\frac{\Delta M}{\Delta x} \simeq 2.3 \times 10^{-4}$$

For x = 14 inches

$$\Delta M \simeq .003$$

Thus the attenuation over the interval in which the velocity is measured is negligible and the convective flow conditions can be calculated directly without any correction for attenuation.

3.3-5 Shock Tube Test Time

The shock tube test time depends on many factors: driver section length, the distance between the driver section and the test section, the distance between the test section and end of the shock tube, the particular gases or gas being used, the strength of the shock, and the local speed of sound. The test time can be determined analytically, however, the actual test time is usually less and thus a series of experiments were performed at various shock strengths to determine the actual test time. This was accomplished by putting the output of the pressure pickups into a Tektronix oscilloscope and photographing the traces. The first pressure pickup started the sweep of the oscilloscope. A typical trace is shown in Fig. 13. The test time extends from the instant of pressure increase to

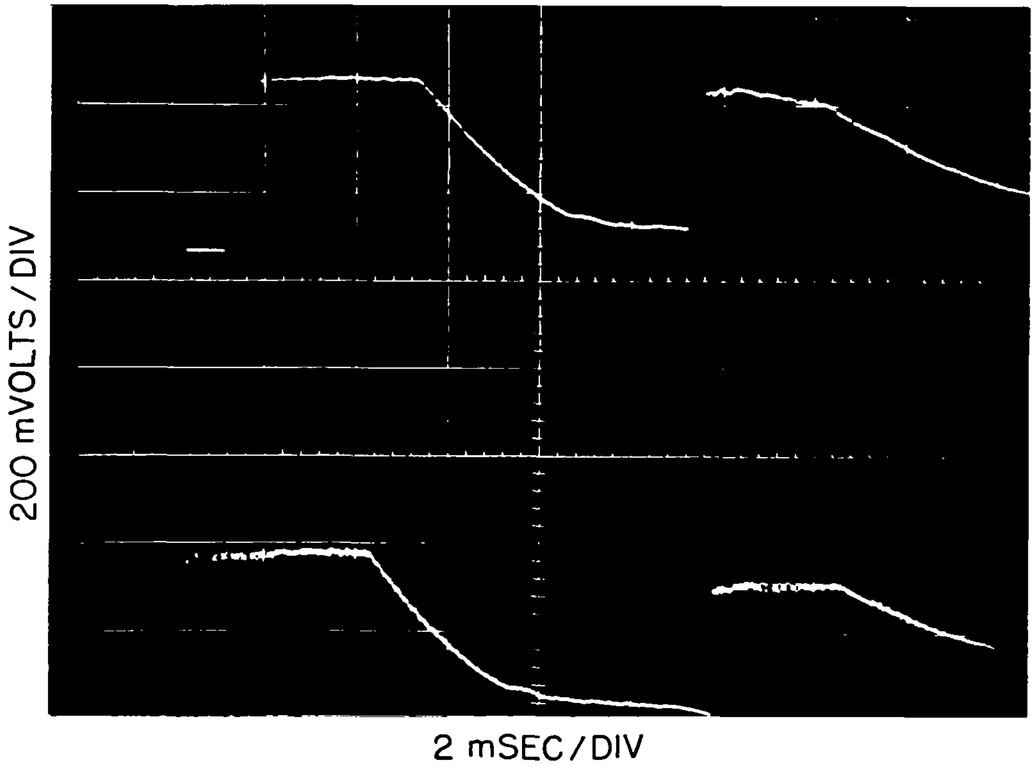

Figure 13. Shock Tube Test Time

the onset of the rarefaction wave and from the above figure is 4.4 milliseconds. The second pressure pulse is from the reflected shock wave. The shortest run time that was recorded over the desired range of shock strengths was 4.2 milliseconds. Thus all of the experimental runs were made in 4.2 milliseconds or less.

IV. DATA REDUCTION AND ERROR ANALYSIS

4.1 RANGE OF EXPERIMENTAL MEASUREMENTS

The experimental study consisted of determining the drag coefficient of non-burning particles under unsteady flow conditions. For all the experimental runs, the relative Mach number of the flow was always less than .3. The $M_R/\sqrt{Re}$ was such that the flow was always in the continuum regime. The Reynolds number ranged from 150 to 1700.

Three different types of particles were used in the study: glass beads, Winchester Western HP 295 ball powder, and synthetic sapphire balls. The superbrite glass beads were obtained from Reflective Products Division of the Minnesota Mining and Manufacturing Company. The glass beads for the most part were spherical; however, some discretion was needed in examining the photographs of the glass beads to sort out the few beads which were not spherical. The Winchester Western HP 295 ball powder likewise was mostly spherical, but again, some selection of data was necessary to eliminate the non-spherical powder. The precision-lapped sapphire balls, obtained from Industrial Tectonics, Inc., were very spherical (within 0.000010). The balls are also uniform in their diameter (± 0.0001 inches), and their surface finish is precise, 1.5 microinches. A table listing some of the particle characteristics appears below:

TABLE I

Type of Particle	Density (gm/ cc)	Size Range or Exact Size
Superbrite Glass Beads	2.49	$150 \bar{\mu} - 250 \bar{\mu}$
Winchester-Western HP 295 Ball Powder	1.67	$280 \bar{\mu} - 350 \bar{\mu}$
Sapphire Balls	3.978	$396.8 \bar{\mu}$

The density of the Superbrite glass beads were obtained experimentally using a Beckman Air Comparison Pycnometer.

4.2 REDUCTION OF EXPERIMENTAL DATA

From each experimental run the following variables are needed for the determination of C_D and Re

1. particle diameter
2. convective flow velocity
3. convective gas density
4. gas viscosity in the convective flow regime
5. particle velocity
6. particle acceleration.

As mentioned previously, the particle diameter is obtained by viewing its image on the film under a microscope. Knowing the camera and microscope magnification factors, the particle diameter is obtained directly.

The convective flow velocity and gas density are obtained from the normal shock relations knowing the shock speed, the temperature of the undisturbed gas, and the pressure of the undisturbed gas in the test section. The temperature in the convective region is likewise given by the normal shock relations. The viscosity values for air at various temperatures were obtained from air viscosity tables of the National Bureau of Standards(16). For small temperature ranges, i.e., $\Delta T \sim 25^{o}R$, the viscosity versus temperature curve is linear. Thus, a series of curves of viscosity versus temperature were plotted for different temperature ranges from the above table. Linear viscosity relationships versus temperature were obtained from these curves for each temperature range so that the viscosity could be solved for analytically. The remaining two variables which must be found for each particle are the velocity and acceleration.

The particle distance versus time history is recorded by taking five photographs on the rotating drum camera at equal time intervals. From these photographs, the particle velocity and acceleration must be obtained.

4.3 METHOD OF DATA REDUCTION

The simplest technique for the reduction of the x versus t data would be to set up a difference table. If this method was used, one would obtain the velocity of the particle from the first difference and the particle's acceleration from the second difference. The main disadvantage of the above method is that each second difference depends on three position measurements, and is very sensitive to any errors in these measurements. Another disadvantage is that an average acceleration and velocity is obtained rather than an instantaneous value. It would be more accurate to fit the position data with a polynominal. Since there are five position points, the highest order polynominal which can be fitted to the points is a fourth order polynominal which would pass through each position point. Thus, any measurement error in the position data would be amplified when the acceleration was obtained by differentiating the analytic x versus t expression twice, since a fourth order polynomial would pass through every point.

A second order polynomial could be used to fit the position data. However, this implies that the force on the particle is a constant. The velocity relative to the particle is actually changing with time and thus the force on the particle is changing with time. The remaining choice is a third order polynominal. By using the third order fit, the final curve would not be forced to pass exactly through the position data and thus some measurement error could exist without affecting the final result drastically. A least square method was used to fit a third order curve through the five position points. Once the analytic expression was obtained, the velocity and acceleration of the particle with respect to inertial space was obtained by differentiating the x versus t expression. The time which was substituted in the analytic expression for x was that which corresponded to the third picture. It was felt that the second derivative was more correct near the center point of the x versus t expression than at the times corresponding to the first or fifth pictures.

The data reduction process for the most part is handled by an IBM 7090 computer program. The data which is put into the computer program for each run is as follows:

1. Run number
2. Particle number
3. Diameter of particle on film
4. Position data; x_0, x_1, x_2, x_3, x_4
5. Atmospheric pressure
6. Initial temperature
7. Initial test section pressure
8. Oscillator frequency
9. Microsecond timer reading
10. Magnification
11. Density of particles

With the above data the computer calculates ρ_2, T_2, U_2, and μ_2; solves for the coefficients of the third order polynomial; then differentiates this expression to obtain the particle velocity and acceleration. Finally, it solves for C_D and Re and prints this and other pertinent data on the output page.

A second data reduction technique which calculates a mean C_D was used to check the third order method results as described below. The particle acceleration and velocity can be written as

$$\alpha = \frac{d^2x}{dt^2} = \ddot{x} \qquad V_p = \frac{dx}{dt} = \dot{x}$$

The equation for C_D can be written as

$$B(U_2 - \dot{x})^2 = \ddot{x} \tag{8}$$

where

$$B = \frac{3\rho_2 C_D}{4\rho_p d}$$

Let $\dot{x} = p \; \ddot{x} = dp/dt$. Equation (8) becomes

$$\frac{dp}{(U_2 - p)^2} = Bdt \tag{9}$$

If we assume that over the time interval of interest B is a constant we may integrate Eq. (9). The values of p and x at limits of the integral are

$$t = 0 \qquad p = p_o \qquad x = x_o$$

$$t = t \qquad p = p \qquad x = x$$

Equation (9) becomes

$$- \int_{p_o}^{p} \frac{d(U_2 - p)}{(U_2 - p)^2} = B \int_{o}^{t} dt$$

Performing the integration and substituting the limits

$$p = U_2 - \frac{1}{Bt + \frac{1}{U_2 - p_o}} = \frac{dx}{dt} \qquad (10)$$

The above may be rewritten as

$$\int_{x_o}^{x} dx = \int_{o}^{t} U_2 \, dt - \frac{1}{B} \int_{o}^{t} \frac{d\left[B\left(U_2 - p_o\right)t + 1\right]}{\left[B\left(U_2 - p_o\right)t + 1\right]}$$

Integrating and substituting in for the limits one has

$$x = x_o + U_2 t - \frac{1}{B} \ln \left[B(U_2 - V_{p_o}) t + 1\right] \qquad (11)$$

A least squares technique is used on the position data to solve for the coefficients of Eq. (11), i.e., x_o, B, and V_{p_o}. Once these have been evaluated, $\overline{C}_D$ can be obtained from B. The particle velocity, V_p, was calculated from Eq. (10) using the time corresponding to the third picture. Knowing V_p, U_2, d, ρ_2, and μ_2, the Reynolds number, Re_2, can be calculated. These calculations have also been programmed for the computer.

The $\overline{C}_D$ method assumes that the C_D is constant over the time interval of the test, an approximately true assumption in the actual case since for a typical run $\Delta C_D / C_D \simeq 1.1 \times 10^{-2}$ over the test-time interval.

4.4 TYPICAL EXAMPLE OF DATA REDUCTION

Figure 14 shows five sequential pictures of a typical run (Run 50E) where the particles are being accelerated by the convective flow behind a shock. The x versus t measurements were made using a ruler graduated in 0.01 of an inch in conjunction with an Edmund 12-power comparator. With this system it was possible to estimate readings on the scale to 0.003 of an inch.

Various information obtained from Run 50E for the data reduction is listed below:

$M = 3.10$

$t_p = 6.812 \times 10^{-4}$ sec

$d = 5.166 \times 10^{-4}$ ft

$T_{atm} = 76.40^{\circ}F$

$P_{atm} = 29.10$ inches Hg

$P_1 = 18.28$ inches Hg

$t_m = 945.0 \times 10^{-6}$ sec

The above data when fed into the two computer programs gave the following results

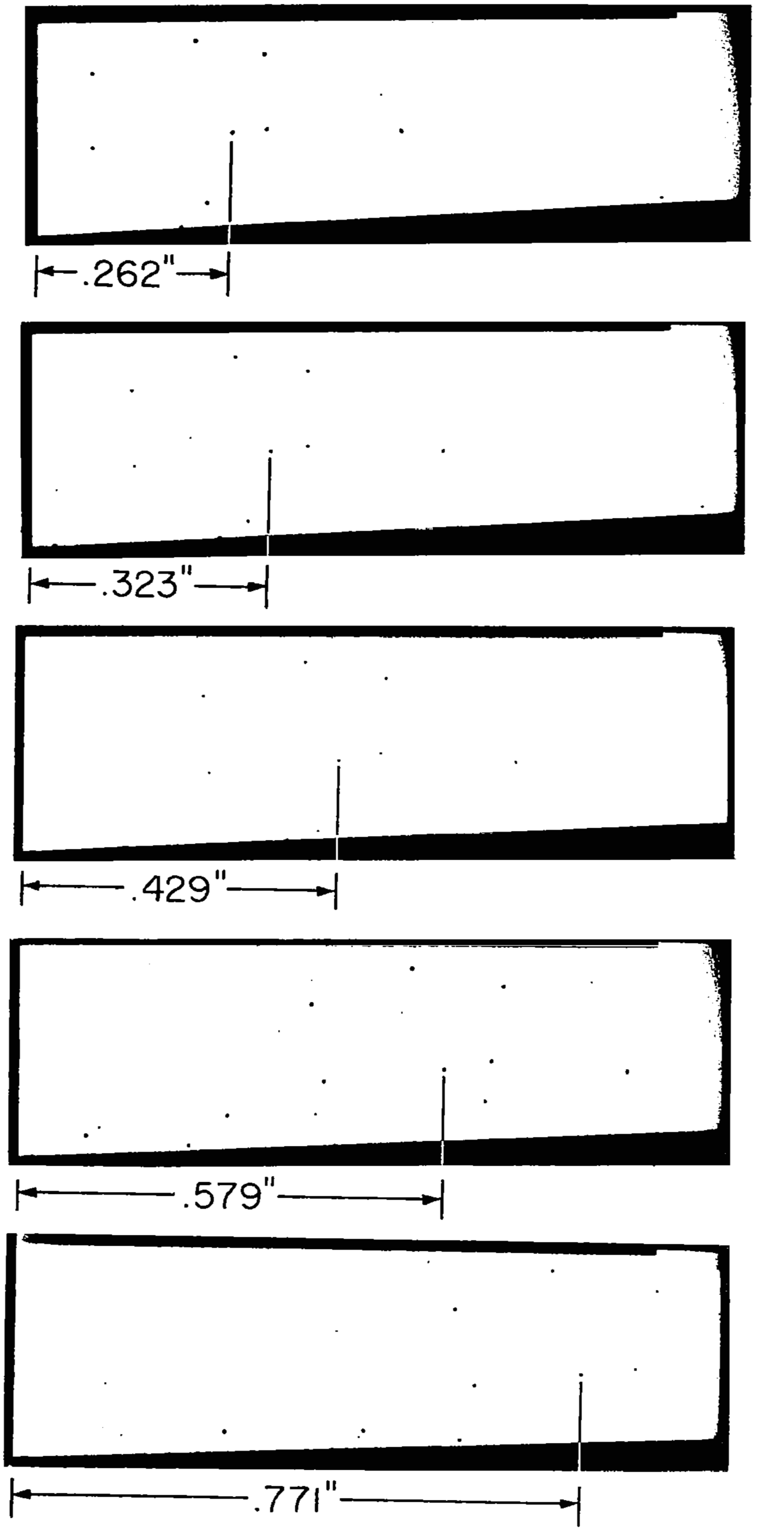

Figure 14. Typical Example of x Versus t Data of a Particle

$M_1 = 1.088$

$U_2 = 159.14$ ft/sec

$\rho_2 = .0519$ lbs/ft^3

$a_1 = 1135.0$ ft/sec

$a_2 = 1166.9$ ft/sec

$P_2 = 1568.8$ lbs/ft^2

$\mu_2 = 1.287 \times 10^{-5}$ lb/ft, sec

From this point on the method of data reduction by the computer programs differed. As mentioned previously, the first program used a third order fit to the x versus t data. A graph of the third order fit for Run 50E appears in Fig. 15. The particle's velocity and acceleration are obtained by differentiating the analytic expression for x versus t once and twice respectively. This expression for the particular particle in question is

$$x = 4.605\ t + 4.223 \times 10^3\ t^2 - 7.045 \times 10^4\ t^3$$

The time which was substituted in for the velocity and acceleration is that which corresponds to the third picture and is

$$t_2 = 1.36 \times 10^{-3} \text{ seconds}$$

The velocity and acceleration corresponding to t_2 is

$$V_p = 15.72 \text{ ft/sec}$$

$$\alpha = 7869.35 \text{ ft/sec}^2$$

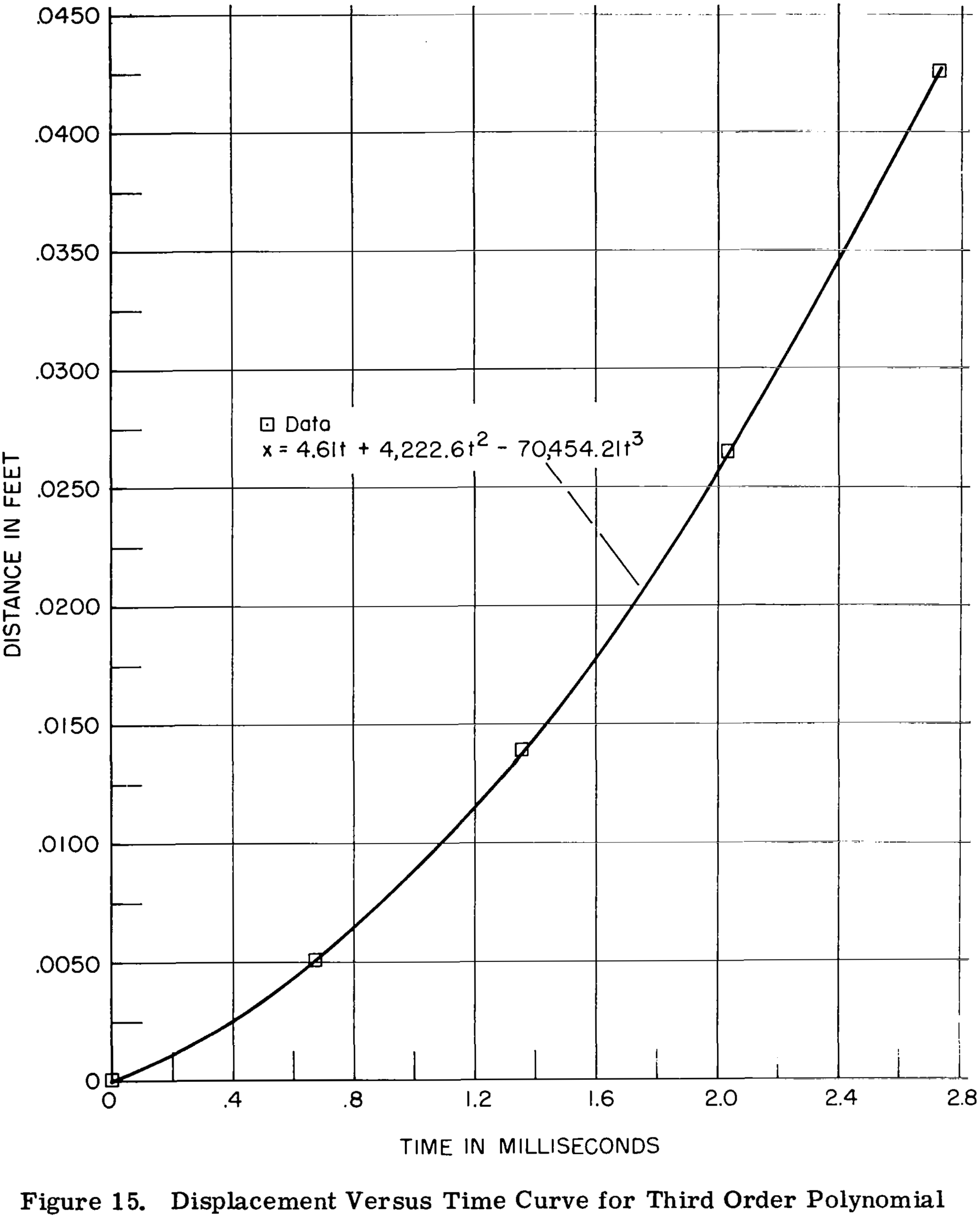

Figure 15. Displacement Versus Time Curve for Third Order Polynomial

When all of the above values are put into the equations for C_D and Re one has

$$C_D = .7926$$

$$Re = 298.81$$

The second computer program solves by the method of least squares for the unknown constants x_o, B, and V_{p_o} in Eq. (11). Once these quantities are known $\overline{C}_D$ and Re_2 are determined. For this sample run one gets

$$\overline{C}_D = .7892$$

$$Re_2 = 299.39$$

In the present use, and in the evaluation of other data, the two methods of data reduction were found to be in substantial agreement.

4.5 GENERAL EQUATIONS FOR DETERMINING PROBABLE ERROR

In order to assess the validity of the experimental data an error analysis must be performed. As can be seen from Eq. (5), C_D is a function of the following independent variables; ρ_p, α, d, ρ_2, U_2, and V_p. The probable error in C_D can be written as$^{(17)}$

$$P(C_D) = \left\{ \left(\frac{\partial C_D}{\partial \rho_p}\right)^2 (\delta \rho_p)^2 + \left(\frac{\partial C_D}{\partial \alpha}\right)^2 (\delta \alpha)^2 + \left(\frac{\partial C_D}{\partial d}\right)^2 (\delta d)^2 + \left(\frac{\partial C_D}{\partial \rho_2}\right)^2 (\delta \rho_2)^2 + \left(\frac{\partial C_D}{\partial U_2}\right)^2 (\delta U_2)^2 + \left(\frac{\partial C_D}{\partial V_p}\right)^2 (\delta V_p)^2 \right\}^{1/2} \qquad (12)$$

Performing the necessary differentiation and substituting into Eq. (12) the probable error in C_D becomes

$$\frac{P(C_D)}{C_D} = \left\{ \left(\frac{\delta \rho_p}{\rho_p}\right)^2 + \left(\frac{\delta \alpha}{\alpha}\right)^2 + \left(\frac{\delta \rho_2}{\rho_2}\right)^2 + 4\left(\frac{\delta U_2}{U_R}\right)^2 + 4\left(\frac{\delta V_p}{U_R}\right)^2 + \left(\frac{\delta d}{d}\right)^2 \right\}^{1/2} \tag{13}$$

The probable deviation or errors in ρ_p, α, d, and V_p can all be estimated or obtained directly from the data. However, the errors in U_2 and ρ_2 must be evaluated from the normal shock relationships in conjunction with C_s, a_1, and P_1, i.e.,

$$U_2 = \frac{2\left(C_s^{\ 2} - a_1^{\ 2}\right)}{(\gamma + 1)\, C_s} \tag{14}$$

$$\rho_2 = \frac{\gamma\,(\gamma + 1)\, P_1\, C_s^{\ 2}}{a_1^{\ 2}\left[(\gamma - 1)\, C_s^{\ 2} + 2a_1^{\ 2}\right]} \tag{15}$$

In all the calculations $\gamma = 1.4$, δU_2 and $\delta \rho_2$ are obtained by taking differentials of Eqs. (14) and (15). The actual values of δU_2 and $\delta \rho_2$ for a particular run are then obtained by substituting in the numerical values for C_s, a_1, and P_1. These values can be put into Eq. (13) with the other deviations and the probable error in drag coefficient, $P(C_D)$, for a particular case can be obtained.

From Eq. (6) the probable error in Re, P(Re), can be written

$$P(\mathrm{Re}) = \left\{ \left(\frac{\partial \mathrm{Re}}{\partial \rho_2}\right)^2 (\delta \rho_2)^2 + \left(\frac{\partial \mathrm{Re}}{\partial U_2}\right)^2 (\delta U_2)^2 + \left(\frac{\partial \mathrm{Re}}{\partial V_p}\right)^2 (\delta V_p)^2 + \left(\frac{\partial \mathrm{Re}}{\partial d}\right)^2 (\delta d)^2 + \left(\frac{\partial \mathrm{Re}}{\partial \mu_2}\right)^2 (\delta \mu_2)^2 \right\}^{1/2} \tag{16}$$

After differentiating Eq. (6) and substituting the results into Eq. (16) P(Re), becomes

$$\frac{P(\mathrm{Re})}{\mathrm{Re}} = \left\{ \left(\frac{\delta \rho_2}{\rho_2}\right)^2 + \left(\frac{\delta d}{d}\right)^2 + \left(\frac{\delta \mu_2}{\mu_2}\right)^2 + \left(\frac{\delta U_2}{U_R}\right)^2 + \left(\frac{\delta V_p}{U_R}\right)^2 \right\}^{1/2} \tag{17}$$

As in the case of C_D,the deviations δV_p, δd, and $\delta \mu_2$ can be estimated or obtained directly from the data. The deviations $\delta \rho_2$ and δU_2 have been determined. Thus for a particular run the probable error in Reynolds number can be obtained using Eq. (17).

4.6 TYPICAL EXAMPLE OF PROBABLE ERROR

The same run which was used in the data reduction section as an example run will be used in determining the probable error in C_D and Re, namely Run 50E. The necessary data from Run 50E is given below:

$\bar{\rho}_p = 2.475$ gm/cc $\qquad V_p = 15.72$ ft/sec

$\alpha = 7869.3$ ft/sec^2 $\qquad C_s = 1234.5$ ft/sec

$d = 5.166 \times 10^{-4}$ ft $\qquad a_1 = 1135.0$ ft/sec

$\rho_2 = .0519$ lb/ft $\qquad P_1 = 1292.8$ lb/ft^2

$U_2 = 159.14$ ft/sec $\qquad$ Time $= 945.0 \times 10^{-6}$ sec

$U_R = 143.43$ ft/sec $\qquad \mu_2 = 1.2868 \times 10^{-5}$ lb/ft sec

The probable error in C_D will be computed first. The first term in Eq. (13) is $\delta\rho_p/\rho_p$. The volume of the glass beads was found by using a Beckman model 930 air comparison pycnometer. A 10 c.c. or larger sample of beads is needed for an accurate volume determination. Once the volume was determined the sample was weighed on a beam balance in order to obtain the average density. The $\delta\rho_p$ and average density, $\bar{\rho}_p$ using the above technique was

$$\delta\rho_p = .050 \text{ gm/cc}$$

$$\bar{\rho}_p = 2.475 \text{ gm/cc}$$

from which

$$\left(\frac{\delta\rho_p}{\bar{\rho}_p}\right)^2 = 4.08 \times 10^{-4}$$

Consider the second term in Eq. (13), $\delta\alpha/\alpha$. The probable error in determining acceleration was attributed only to incorrect particle displacement measurements. Typical displacement errors (± .003 inches) were incorporated into the original measurements of x versus t. This new data was then run through the computer program for data reduction to find the new value for acceleration. Doing this the deviation in acceleration for Run 50E is

$$\delta \alpha = 274.5 \text{ ft/sec}^2$$

$$\left(\frac{\delta \alpha}{\alpha}\right)^2 = 12.18 \times 10^{-4}$$

The next term is $\delta d/d$. The deviation in particle diameter was considered due only to the error in estimating the exact location of the particle's edge. The deviation for the diameter was

$$\delta d = .151 \times 10^{-4} \text{ ft}$$

$$\left(\frac{\delta d}{d}\right)^2 = 8.52 \times 10^{-4}$$

The deviation in the particle's velocity, δV_p, was calculated as being due to incorrect displacement measurements as in the acceleration case. The method for determining δV_p was entirely analogous to that of $\delta \alpha$ as mentioned above, and for Run 50E δV_p is

$$\delta V_p = .24 \text{ ft/sec}$$

$$4\left(\frac{\delta V_p}{U_R}\right)^2 = .11 \times 10^{-4}$$

$\delta \rho_2$ depends on the deviations of C_s, a_1, and P_1. The initial test section pressure, P_1, is read off a mercury manometer and thus δP_1 is rather small.

$$\delta P_1 = 5.17 \text{ lb/ft}^2$$

$$\frac{\delta P_1}{P_1} = .4 \times 10^{-2}$$

The deviation in a_1 is that caused by a change in the temperature and is for Run 50E

$$\delta a_1 = 2 \text{ ft/sec}$$

The deviation in shock speed, C_s, is considered due only to the error in the microsecond timer. It was shown in a previous section that attenuation affects could be neglected. It was also mentioned that since the outputs of the two transducers had the same slopes and both channels of the microsecond timer were calibrated, the measured time would be correct. The deviation due to the error in the microsecond timer is

$$\delta C_s = 1.2 \text{ ft/sec}$$

Substituting in the proper values in $\delta \rho_2$ we have

$$\delta \rho_2 = -.416 \times 10^{-4}$$

$$\left(\frac{\delta \rho_2}{\rho_2}\right)^2 = .645 \times 10^{-6}$$

Similarly δU_2 is obtained and is

$$\delta U_2 = -1.226 \text{ ft/sec}$$

$$4\left(\frac{\delta U_2}{U_R}\right)^2 = 2.92 \times 10^{-4}$$

All of the terms which appear in Eq. (14) have been computed. Putting these terms in Eq. (13) the probable error in drag coefficient is for Run 50E

$$\frac{P(C_D)}{C_D} = 5.28 \times 10^{-2}$$

In calculating the probable error in Reynolds number Eq. (17) must be used. This equation contains the same deviations as those just calculated for C_D plus $\delta \mu_2$. Thus for the Re number case, it is necessary only to find $\delta \mu_2$. $\delta \mu_2$ is caused only by an error in the temperature measurement. This gives $\delta \mu_2$ as

$$\delta \mu_2 = .005 \times 10^{-5} \text{ lb/ft, sec}$$

$$\left(\frac{\delta \mu_2}{\mu_2}\right)^2 = 1.51 \times 10^{-5}$$

Putting $(\delta \mu_2 / \mu_2)^2$ and the other values into Eq. (17) for the probable error in Re for Run 50E we have

$$\frac{P(Re)}{Re} = 3.71 \times 10^{-2}$$

V. RESULTS AND DISCUSSION OF RESULTS

5.1 EXPERIMENTAL RESULTS

The experiments involving the glass beads were all carried out using a magnification of 3.1. Before a particular particle was used, the film record of the x versus t history was checked against the following conditions.

1. Any particle which was closer than five diameters to another particle perpendicular to the direction of motion was not used.
2. Any particle which was within twelve diameters of another particle wake or had another particle within twelve diameters of its wake was not used in the data reduction.
3. If any diaphragm material appeared in any of the five frames, the run was discarded.
4. Only spherical particles were used in the data reduction.
5. Only particles which were sufficiently sharp were used for the data reduction.

Because of the above restrictions, many particles could not be used to obtain C_D versus Re data. Table 2, in the Appendix, is a summary of experimental data for glass beads in incompressible continuum flow. C_D and Re results obtained using both methods of data reduction appear in the table. If the C_D versus Re points are plotted on log-log paper, they appear to fall in nearly a straight line. Thus, a least squares technique was used to fit the C_D versus Re data with an equation of the following form:

$$\log_{10} C_D = A_o + A_1 \log_{10} \mathrm{Re} + A_2 (\log_{10} \mathrm{Re})^2 \tag{18}$$

Other analytical forms were tried for C_D versus Re data, however, none of these other forms fit the data nearly as well as that of Eq. (18). The results which appear in Table 2 are plotted in Figs. 16 and 17 for the two methods of data reduction. The best fit curve for these points is also plotted.

A second series of experimental runs were made with the glass beads at higher shock strengths to begin a study of the influence of compressibility. The results of these runs appear in Table 3. The relative Mach number, M_R, for the flow field about the particles is $.15 \leq M_R \leq .30$. The C_D has increased as much as 50 per cent with respect to similar data which appeared in Table 2. The scatter in C_D for a particular Re has increased approximately 40 per cent. This shift in C_D cannot be attributed to compressibility effects since the relative Mach number, M_R, is still quite low. Likewise the scatter in C_D cannot be explained by differences in experimental technique since the results which appear in Table 3 were obtained in precisely the same manner as the data which appears in Table 2. Thus two more series of experimental runs were made in an

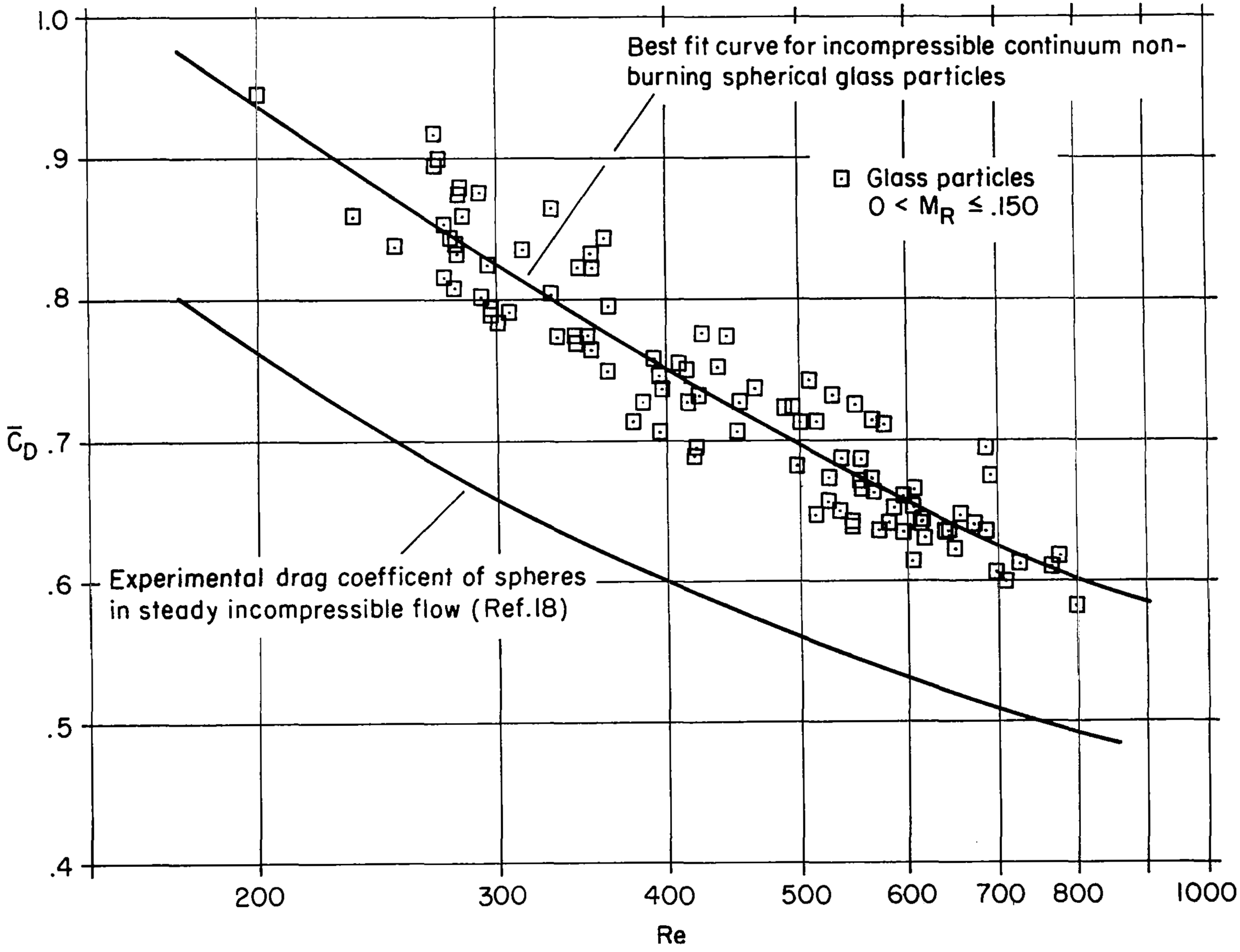

Figure 16. Drag Coefficients Versus Reynolds Number for Third Order Polynomial Data Reduction Technique

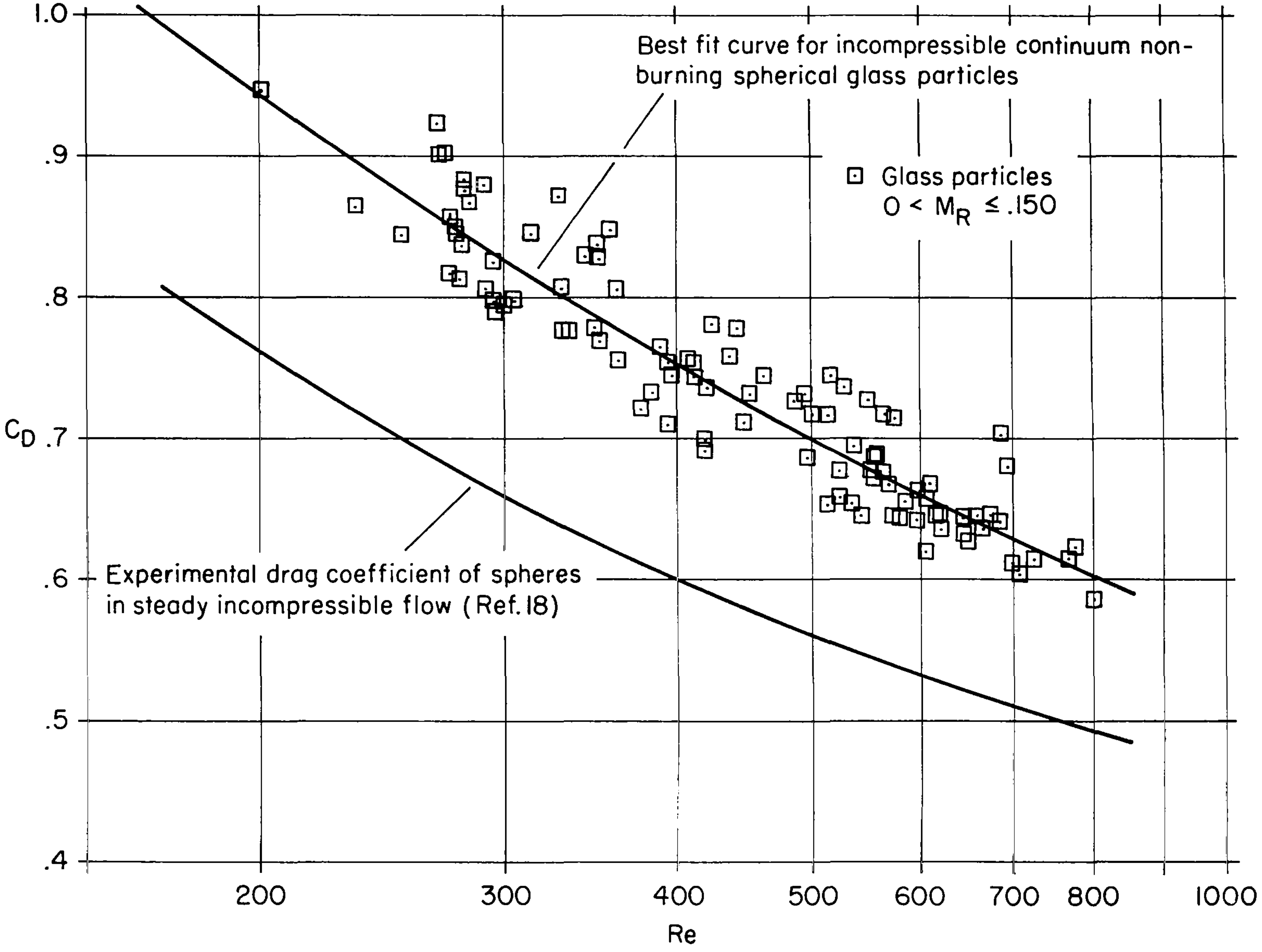

Figure 17. Drag Coefficient Versus Reynolds Number for Mean Drag Coefficient Method

attempt to explain the above results. They were made using the same experimental technique that was used for the data of Tables 2 and 3. The only change was the types of particles that were used, Winchester-Western HP 295 ball powder and sapphire balls. The data summaries for the HP 295 ball powder and sapphire balls appears in Tables 4 and 5 respectively. The results of Tables 3, 4, and 5 are illustrated in Fig. 18.

5.2 SURFACE ROUGHNESS

Figure 18 shows that the scatter in the HP 295 ball powder data is of the same level as that obtained for the higher relative Mach number runs using glass beads. The relative Mach number of the flow about the ball powder, however, was $M_R \leq .124$. Both for the HP 295 ball powder and the higher relative Mach number glass bead data, the average C_D for a particular Reynolds number fell above the best fit curve of the glass beads. In contrast to this, the average C_D for the sapphire runs for a particular Reynolds number falls below the best fit curve of glass beads and does not seem to be a function of the M_R.

As an attempt to explain the varied results which appear in Fig. 18, photomicrographs were taken of the particles. Photomicrographs of $200\,\mu$ glass beads appear in Figs. 19, 20, and 21. Under the relatively low power magnification of Fig. 19, the glass beads appear to have fairly smooth surfaces except for a few bubbles or craters which appear on

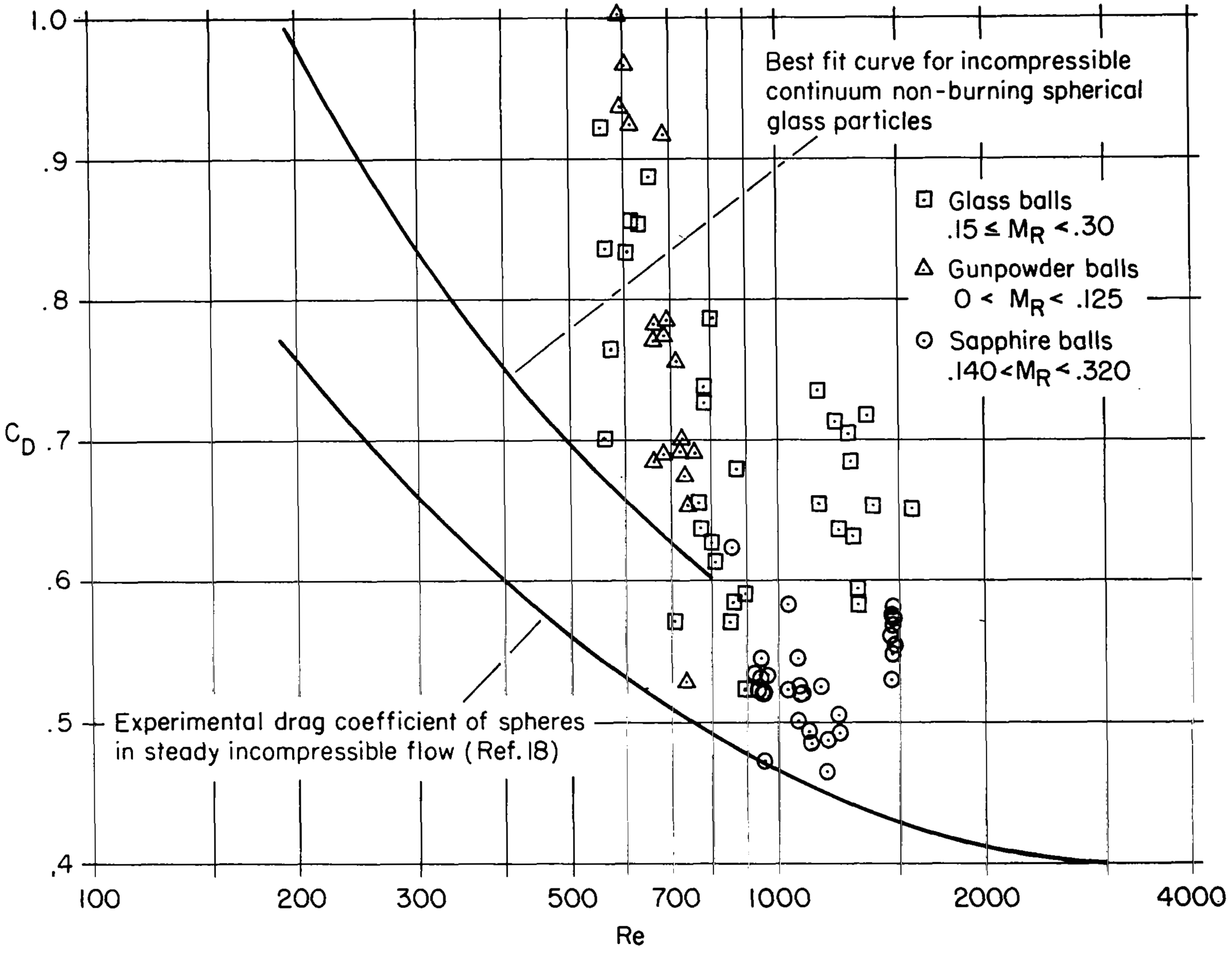

Figure 18. Drag Coefficient Versus Reynolds Number—Glass Particles, Ball, Powder, and Sapphire Balls

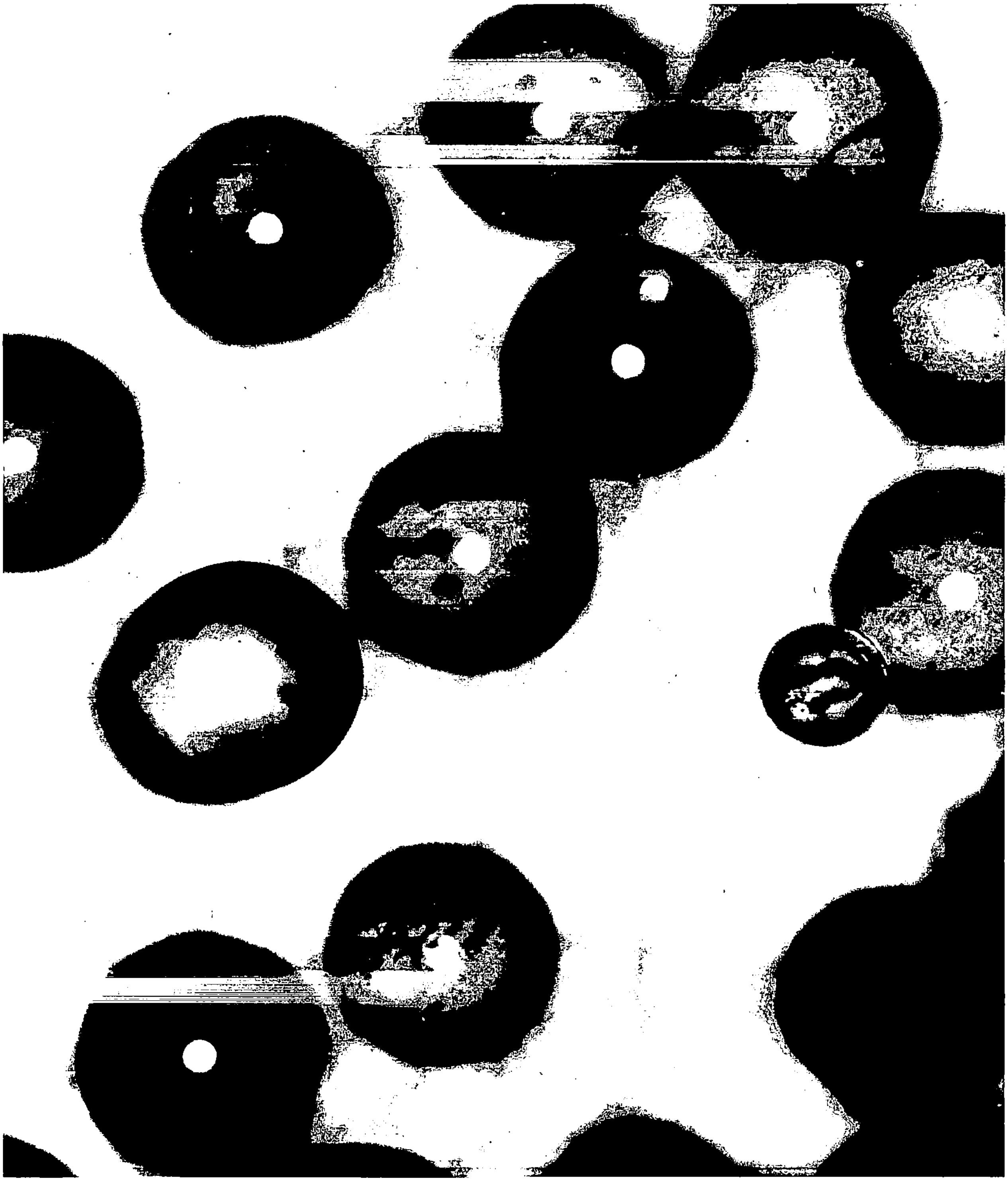

Figure 19. Photomicrograph of Glass Particles, Magnification = 200

Figure 20. Photomicrograph of Glass Particle, Magnification = 1840

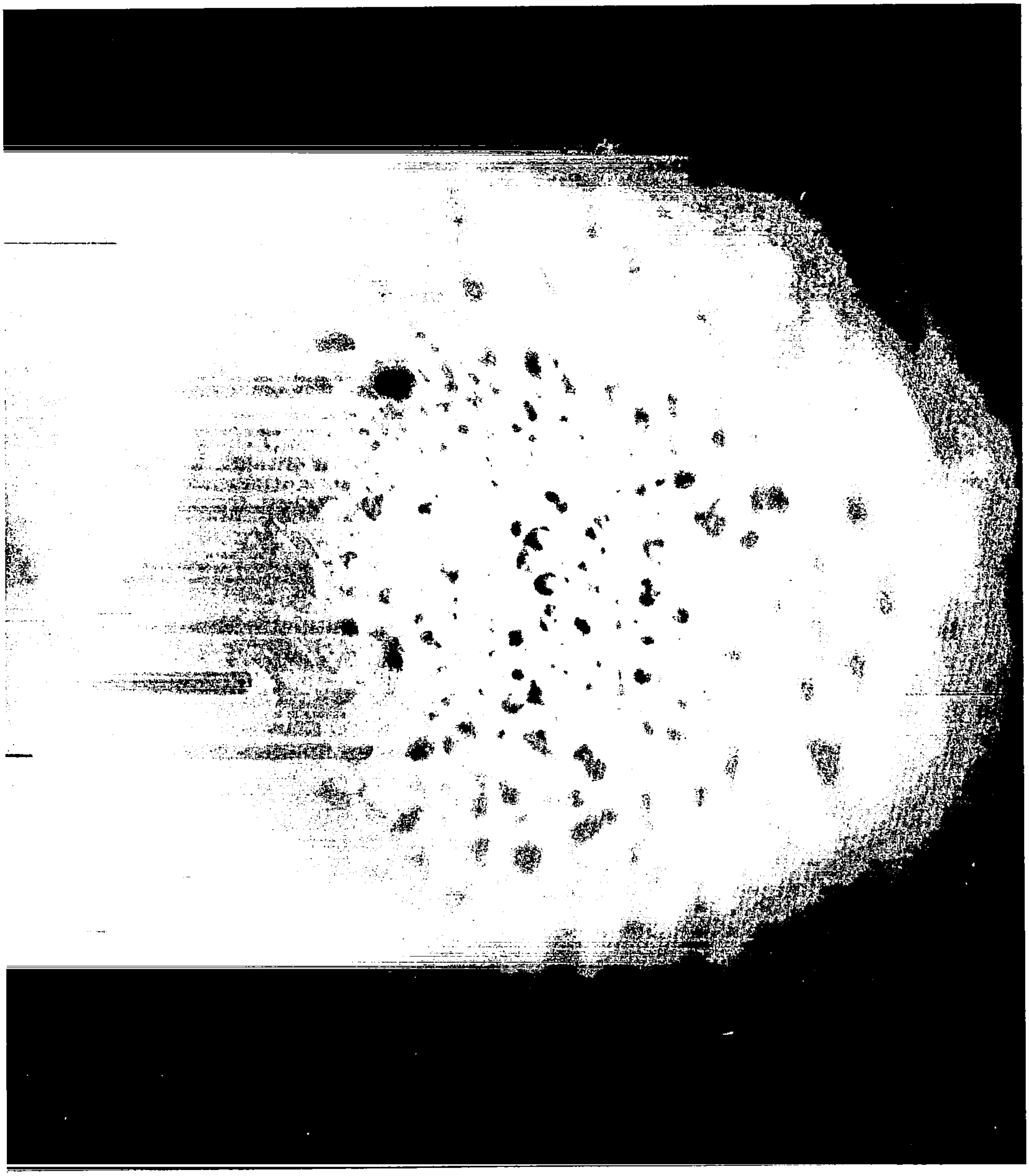

Figure 21. Photomicrograph of Glass Particle, Magnification = 1840

most of the beads. Figure 20 shows a detailed view of these bubbles or craters. These protrusions and craters are quite pronounced relative to the particle diameter. Figure 21 is a detailed view of a portion of the glass bead which is free of the larger surface blemishes. However, this portion of the surface still possesses a considerable amount of roughness relative to the particle diameter. Photomicrographs of HP 295 ball powder appear in Figs. 22, 23, and 24. Figure 22 is a low-power photomicrograph and shows only that the ball powder is spherical with a few surface protrusions. Figure 23 is of intermediate magnification, and it appears from this figure that the entire surface of the ball powder is rough relative to the similar photomicrograph of the glass beads in Fig. 19. Finally, Fig. 24 is a detailed view of the ball powder. Again the surface appears to be rougher than that of glass beads. Photomicrographs of sapphire balls appear in Fig. 25, 26, and 27. Figure 25 is a low-power photomicrograph and indicates only that the sapphire ball is spherical. Figure 26 is a detailed view of a sapphire ball. From this figure it is evident that the sapphire balls have less surface roughness than even the portions of glass that were free of the bubbles or craters. Figure 27 is a photomicrograph of a sapphire ball which was washed in trichloroethylene before the photomicrograph was taken. Almost all of the roughness which appeared in Fig. 26 is missing in Fig. 27. The relative Mach number range for the sapphire was, $.14 \leq M_R \leq .313$

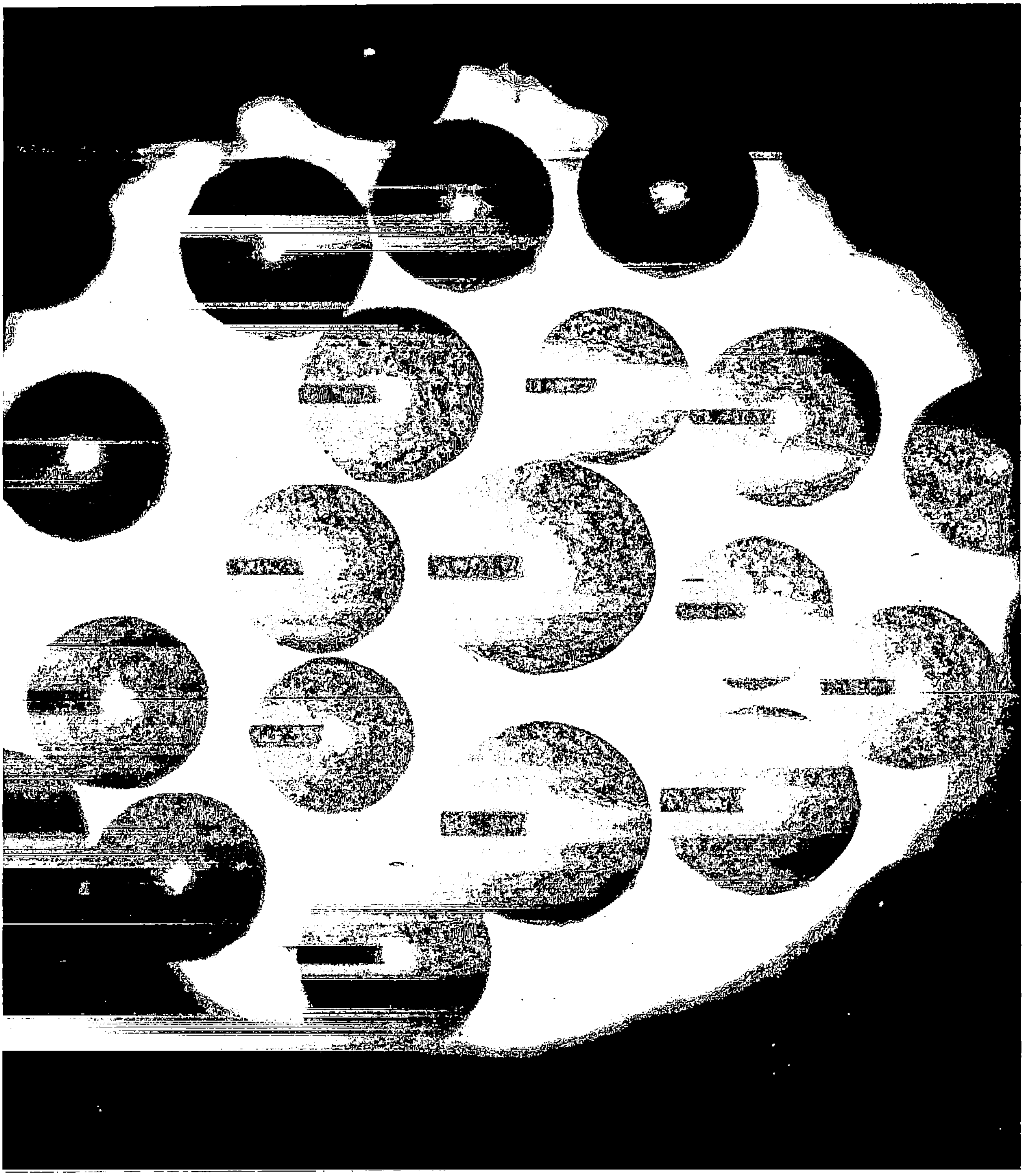

Figure 22. Photomicrograph of HP 295 Ball Powder, Magnification = 110

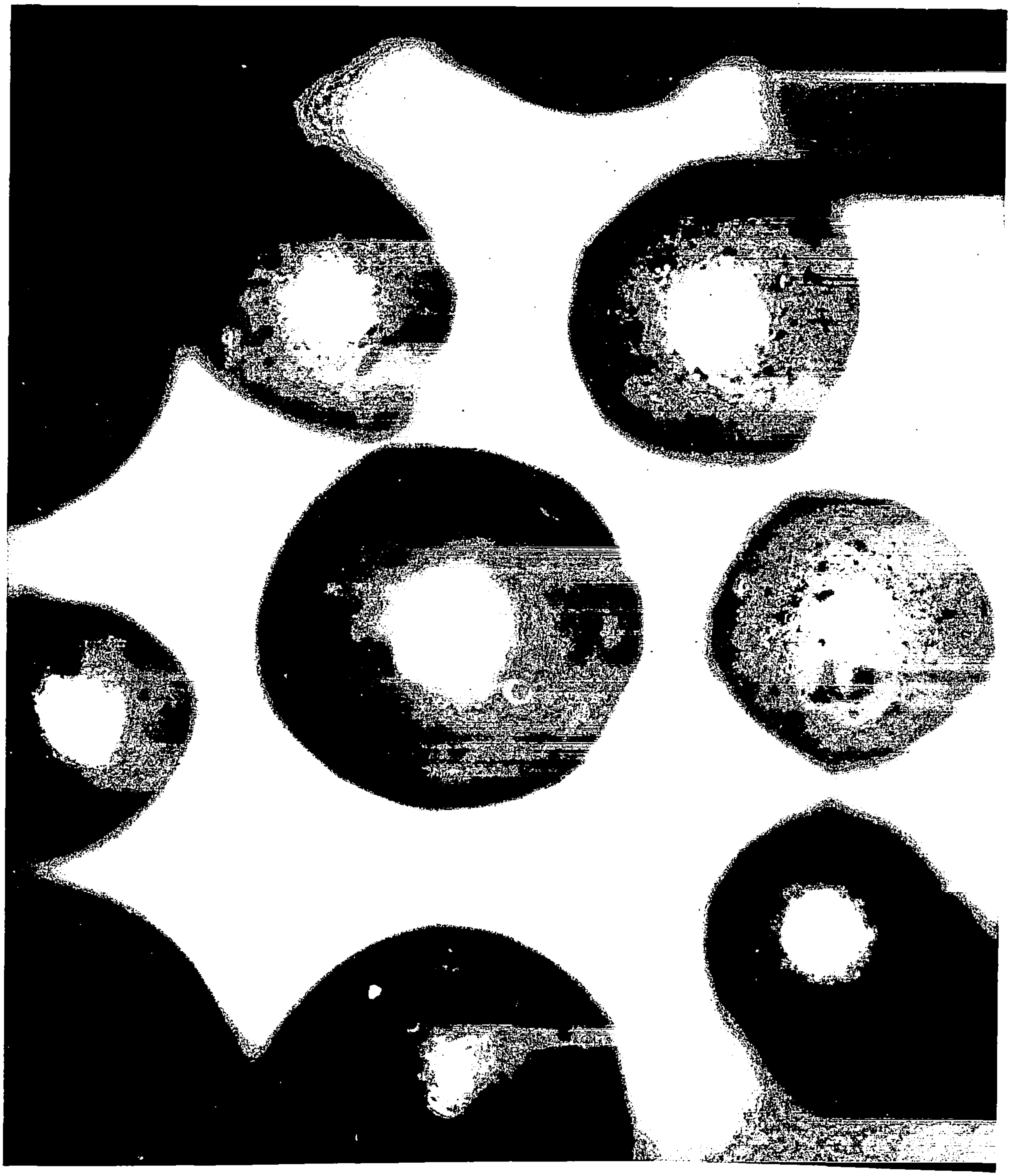

Figure 23. Photomicrograph of HP 295 Ball Powder, Magnification = 190

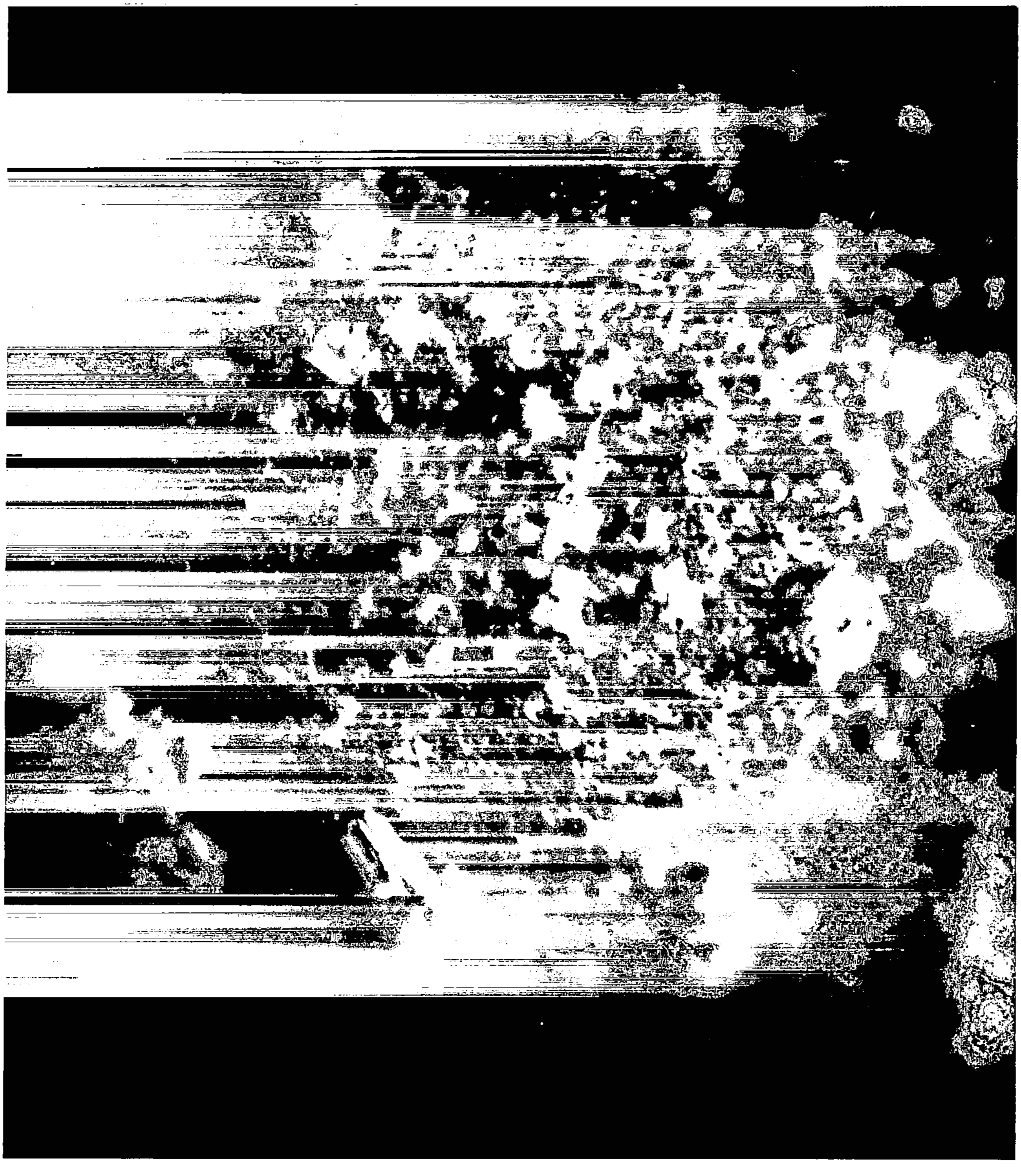

Figure 24. Photomicrograph of HP 295 Ball Powder, Magnification = 1840

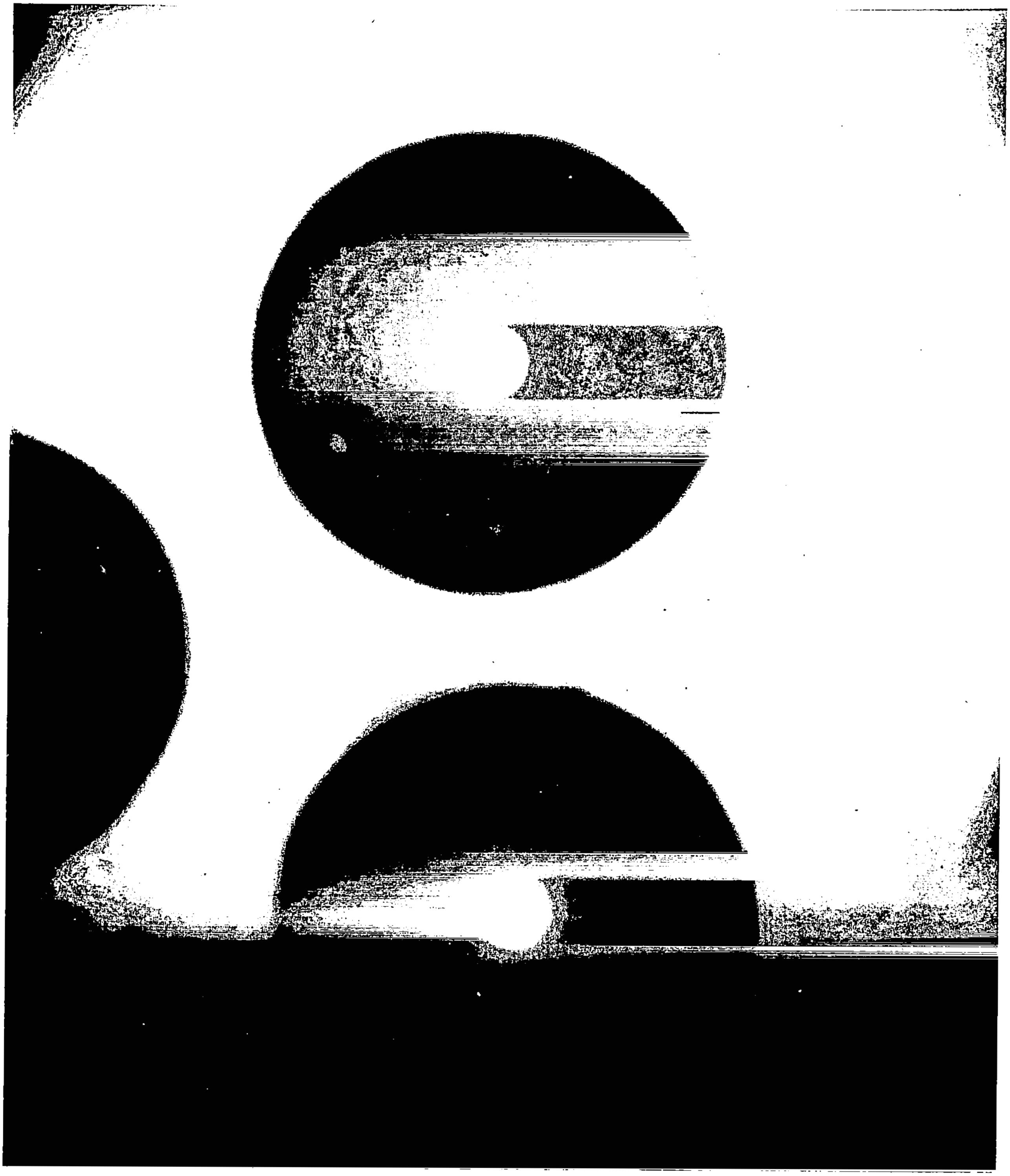

Figure 25. Photomicrograph of Sapphire Balls, Magnification = 202

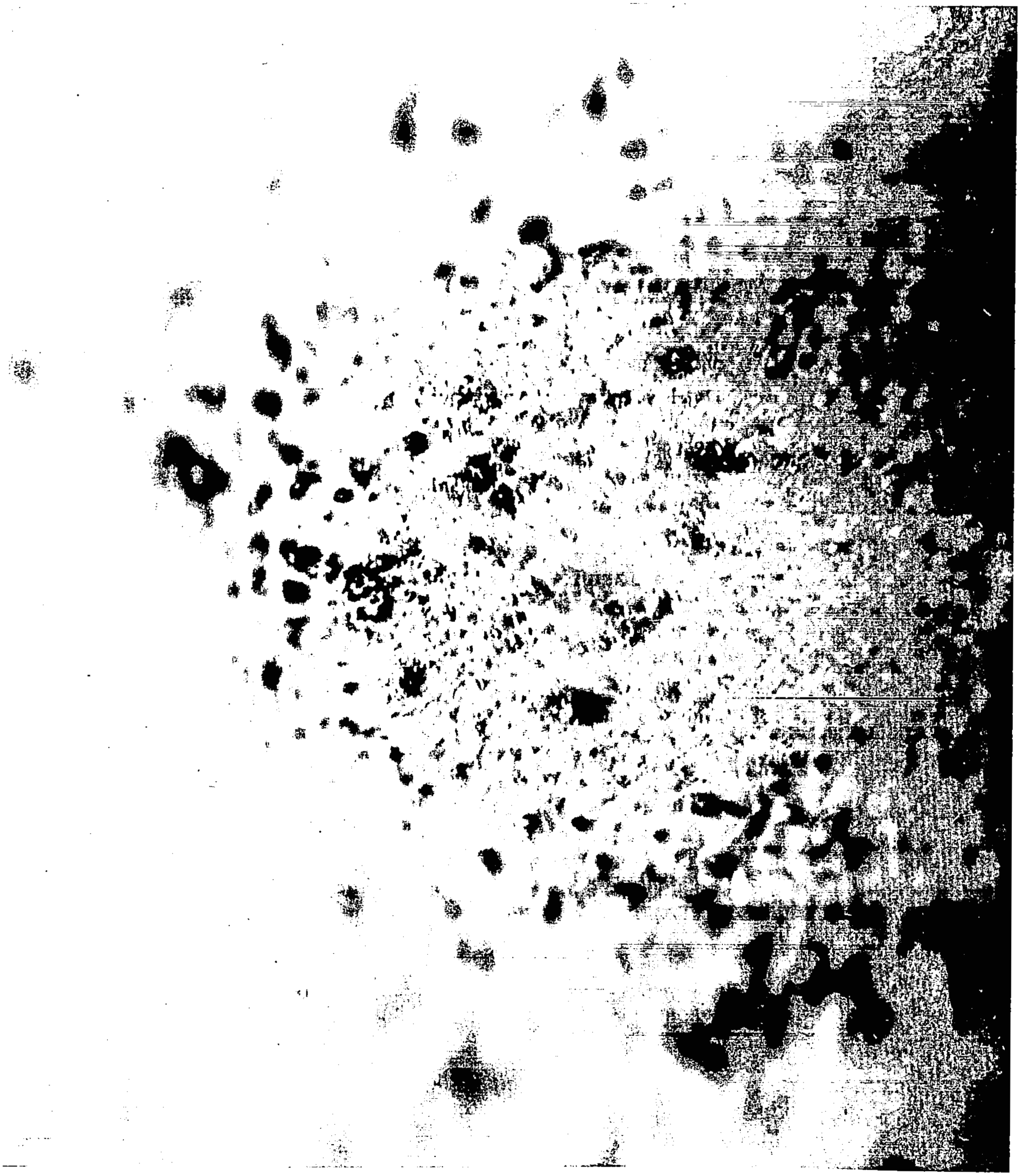

Figure 26. Photomicrograph of Sapphire Ball, Magnification = 1850

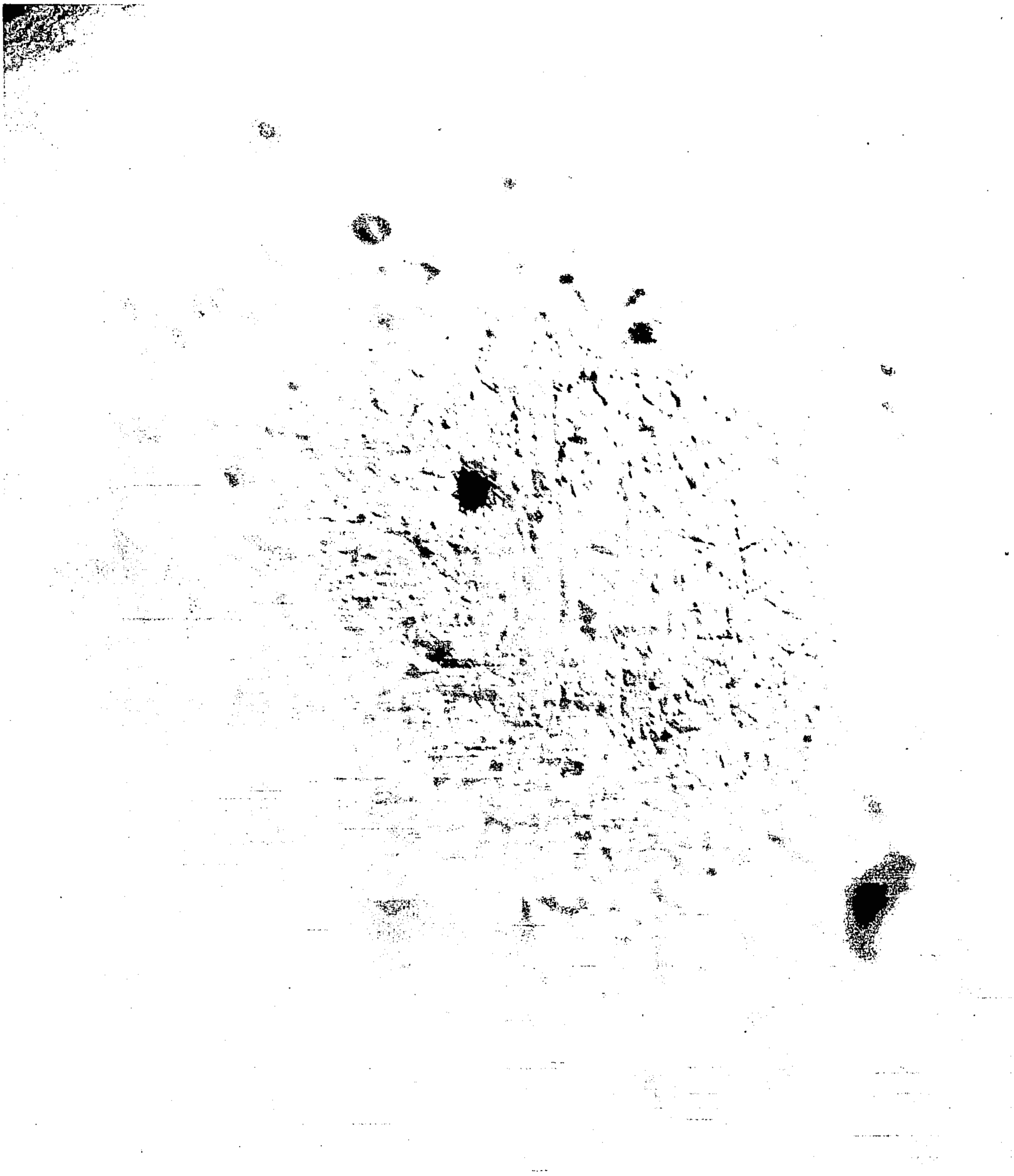

Figure 27. Photomicrograph of a Washed Sapphire Ball, Magnification = 1760

yet none of the violent scatter occurred that was found using both the glass particles and the HP 295 ball powder. As noted earlier, the only differences between the various types of particles and the experimental runs involving these particles is the particle's surface finish.

5.3 UNSTEADINESS IN THE BOUNDARY LAYER AND WAKE

The interaction of the shock wave with a particle is analogous to the impulsive motion of a sphere in a fluid in that the particle impulsively sees and is acted upon by the convective flow velocity behind the shock front. In impulsive motion a certain amount of time is needed for the boundary layer and the wake to reach a quasi-steady condition. In order to determine the time it takes for the boundary layer to become quasi-steady, a diffusion time may be defined as the time required for a sudden change to spread by the process of molecular or turbulent diffusion(19). The diffusion time may be taken as δ^2/ν where δ is the boundary layer thickness and ν is the kinematic viscosity. The experimental displacement thickness at the 90° point on a circular cylinder is(18)

$$\frac{\delta^*}{R}\frac{U_\infty R}{\nu} = .8$$

If we assume the following values for R, U_∞, and ν

$$R = 3.28 \times 10^{-4} \text{ ft}$$

$$\nu = 1.611 \times 10^{-4} \text{ ft}^2/\text{sec}$$

$$U_\infty = 100 \text{ ft/sec}$$

Then $\delta^*_{90^o}$ becomes

$$\delta^*_{90^o} = 1.841 \times 10^{-5} \text{ ft}$$

The diffusion time may be approximated using the displacement thickness for a cylinder and is

$$\frac{\delta^2}{\nu} = 2.12 \times 10^{-6} \text{ sec}$$

The minimum time from shock front passage over the particles until the first picture was taken was always greater than 100 microseconds. The diffusion time as computed above is only two per cent of this time and thus by the time the experimental data is taken, the boundary layer should be quasi-steady.

Experimental work on impulsive flow about cylinders has been done by Schwabe(20) and very recently by Sarpkaya(21). Sarpkaya's experiments involved the impulsive flow of water about circular cylinders. He found that the drag coefficient initially rises above the steady state case due to the formation of the vortices and then decays back to the steady state case once the vortex flow has become established. He found that his C_D data correlated with a non-dimensional time τ. The drag coefficient had returned to the steady state result when $\tau \approx 28$. τ is defined as

$$\tau = \frac{U_\infty t_w}{R}$$

where U_∞ = flow field velocity

t_w = time

R = radius of cylinder

For $U_\infty = 100$, $R = 3.28 \times 10^{-4}$ ft, and $\tau = 28$ then t_w becomes

$$t_w = 91.8 \times 10^{-6} \text{ sec}$$

It might be noted that since the wake formation time is an order of magnitude larger than the boundary layer formation time, then in unsteady flow problems, the wake formation time dominates. Since t_w is less than 100 microseconds, which is the time between when the shock passes the particles to when the first picture is taken, the wake flow field has reached a quasi-steady condition before the data is taken. Thus both the boundary layer and the wake have become quasi-steady before any experimental data is taken.

5.4 TURBULENCE IN THE FREE STREAM

Free stream turbulence can cause a considerable shift in C_D for a particular Re as can be seen from Torobin's and Gauvin's(12) results which appear in Fig. 2. A literature survey yielded no information on turbulence behind a shock wave. Since the shock waves are weak and the convective flow Mach numbers are low, any turbulence which is generated in the boundary layer will not be transmitted into the convective flow. Turbulence will not be generated by the shock front since Schlieren photographs indicated the shock front was plane and perpendicular to the walls of the shock tube. Further, the fact that smooth sapphire balls yielded C_D data close to the steady state curve tends to substantiate a turbulent-free flow field assumption.

5.5 PARTICLE ROTATION

Particle rotation could cause a shift in the drag coefficient of a particle in that on one side of the particle the separation point will move rearward whereas on the other side it will move forward. This will cause the skin friction and the form drag contributions to the drag coefficient to change. Maccoll(22) conducted some experiments to determine the effects of sphere rotation around an axis perpendicular to the flow. These experiments ranged from Reynolds numbers of 6.15×10^4 to 10.7×10^4. C_D fell from .52 to .48 as the ratio of equatori peed,

U_s, to the relative velocity, U_R, increased from 0 to 1. Davies(23) has conducted experiments in the same Reynolds number regime as Maccoll and his results agree with Maccoll's. Pasternak(24) made observations of freely moving spheres and suggests that the ratio of U_s/U is on the order of five per cent. Luthander(25) has measured the drag coefficient of spheres rotating around an axis parallel to the flow direction in the region of the critical Reynolds number. Below the critical Reynolds number, a U_s/U ratio up to two had very little effect on C_D. Garstang(26) and Drazin(27) studied analytically the effects of rotation about the axis parallel to the flow direction for the Stokesian drag regime and found that the drag coefficient remained unaffected by the rotation. Due to the above results that rotation does not change the drag coefficient significantly and since spherical particles are injected in the present study in a manner which does not initiate rotational motion, it is felt that rotational effects are negligible in the present study.

5.6 ACCELERATION EFFECTS

A considerable amount of experimental work has been done on the effects of acceleration on both sphere and cylinder drag. Keim(28), did experiments with accelerating cylinders. He found that the drag coefficient versus Reynolds number data could be correlated by using an acceleration modulus defined as

$$A_c = \frac{\alpha d}{U_R^2}$$

He found that if A_c was on the order of .2 or greater then the effect of acceleration upon the drag coefficient was substantial. Bugliarello$^{(29)}$ determined experimentally the drag coefficient for accelerating spheres. He found his data also correlated with the acceleration modulus, A_c. Crowe$^{(13)}$ showed analytically that

$$\left(\frac{\Delta C_f}{C_f}\right)_{\theta=\frac{\pi}{2}} < -\frac{\pi A_c}{9}$$

where C_f = skin friction coefficient. The acceleration moduli for the present study were of the order of 10^{-4} to 10^{-3}. $\Delta C_f / C_f$ becomes

$$\left(\frac{\Delta C_f}{C_f}\right)_{\theta=\frac{\pi}{2}} < -.35 \times 10^{-3}$$

Thus acceleration effects do not seem to be important in the present study.

VI. CONCLUSIONS

Observations on the drag coefficient of small spherical particles in an incompressible, laminar, non-reacting, continuum flow regime are summarized below:

1. The drag coefficient of small spherical particles in laminar, non-reacting, incompressible flow regime was found to be consistently higher for a particular Reynolds number than the generally accepted steady state value.

2. The C_D of the HP 295 ball powder, for $M_R < .125$, increased as much as 85 per cent and the C_D of glass beads increased significantly, for $.15 < M_R \leq .30$, over the steady state value respectively.

3. The C_D and the scatter in the C_D data of the HP 295 ball powder and the glass beads substantially increased as the relative Mach number increased, even though the relative Mach number was still in a region which is normally considered incompressible.

4. The C_D of smooth sapphire balls fell closer to the steady state curve and did not depend on the relative Mach number nor did the scatter in the C_D data increase as the relative Mach number increased.

5. Photomicrographs of HP 295 ball powder, glass beads, and sapphire balls indicated that the sapphire balls were relatively smooth, the glass beads somewhat rougher, and the HP 295 ball powder quite rough.

It is concluded that surface roughness can cause considerable shift in C_D for small spherical particles in an incompressible, laminar, non-reacting, continuum flow regime. Since one group of particles in solid propellant rocket exhaust is relatively rough, i. e., those metalic particles which are originally cast into the solid propellant, their C_D may be several hundred per cent higher than the steady state results. The other particles in the rocket exhausts are those which are condensed from the combustion products. The C_D of the condensed particles could also deviate appreciably from the steady state value depending upon the relative surface roughness and deformation of the particles. Thus, the use of the steady state C_D curve for velocity lag calculations of particles in rocket nozzles possibly causes considerable error.

This study has only touched upon the regimes a particle encounters in a solid propellant rocket exhaust. Much work is left to be done on the influence of compressibility, burning, and electric charges in the slip-flow, transition, and free molecular regimes.

APPENDIX

TABLE 2

DATA SUMMARY - GLASS BEADS
$0 < M_R \leq .15$

RUN	C_D	Re	M_1	M_R	d ft	α ft/sec^2	U_R ft/sec	$\overline{C}_D$	Re_2
3D-1	.828	344.5	1.067	.096	4.99×10^{-4}	7886.3	111.7	.824	344.3
3D-2	.827	351.0	1.067	.096	5.09×10^{-4}	7699.2	111.6	.823	350.8
4D-1	.774	343.7	1.067	.095	5.04×10^{-4}	7125.7	110.7	.769	342.9
4D-2	.775	341.8	1.067	.095	5.04×10^{-4}	7064.2	110.1	.772	341.6
4D-3	.774	330.8	1.067	.095	4.89×10^{-4}	7229.2	109.8	.771	331.1
5D-1	.769	351.4	1.067	.101	4.84×10^{-4}	8340.0	117.2	.764	351.0
5D-2	.802	362.8	1.072	.101	4.99×10^{-4}	8451.1	117.3	.796	361.8
6D-1	.835	351.2	1.070	.097	5.04×10^{-4}	8014.5	112.8	.831	351.4
7D-1	.754	362.7	1.074	.105	4.79×10^{-4}	8985.1	122.1	.749	362.1
7D-2	.742	396.4	1.075	.106	5.19×10^{-4}	8288.8	123.0	.738	395.9
9D-1	.841	313.7	1.065	.091	4.84×10^{-4}	7313.8	105.6	.836	313.1
9D-2	.805	329.5	1.065	.092	5.04×10^{-4}	6831.8	106.5	.801	329.2
10D-1	.869	329.3	1.070	.096	4.79×10^{-4}	8569.9	111.4	.863	329.2
10D-2	.847	357.8	1.071	.097	5.14×10^{-4}	7970.9	112.7	.843	357.8
11D-1	.763	389.4	1.077	.106	5.04×10^{-4}	8998.0	124.3	.759	389.5
11D-2	.778	349.2	1.077	.105	4.59×10^{-4}	9783.3	122.5	.773	348.9
11D-3	.751	394.1	1.077	.107	5.09×10^{-4}	8801.5	124.6	.747	393.6
12D-1	.756	407.4	1.064	.094	6.10×10^{-4}	5587.8	109.7	.755	407.6
17D-1	.741	508.1	1.071	.103	6.90×10^{-4}	5869.4	120.3	.741	508.8
18D-1	.778	442.6	1.067	.095	6.55×10^{-4}	5489.4	111.0	.774	442.2
27D-1	.779	424.3	1.061	.090	6.70×10^{-4}	4775.1	105.3	.777	424.1
35D-1	.642	543.8	1.081	.116	6.30×10^{-4}	7388.9	135.8	.639	543.2
41D-1	.644	672.7	1.095	.133	6.70×10^{-4}	9322.5	155.5	.641	672.4

TABLE 2 (cont)

RUN	C_D	Re	M_1	M_R	d ft	α ft/sec^2	U_R ft/sec	$\overline{C}_D$	Re_2
43D-1	.621	778.4	1.105	.147	6.90×10^{-4}	10977.3	173.1	.619	778.7
43D-2	.612	766.6	1.105	.147	6.80×10^{-4}	10961.1	172.9	.610	767.6
47D-1	.585	800.1	1.110	.156	6.60×10^{-4}	12375.9	183.7	.582	799.3
49D-2	.603	709.0	1.100	.141	6.60×10^{-4}	10108.8	165.5	.600	708.7
51D-1	.614	723.9	1.110	.146	6.48×10^{-4}	11350.4	171.4	.612	724.7
56D-1	.610	699.3	1.100	.140	6.60×10^{-4}	9982.2	163.9	.607	699.1
58D-1	.646	616.4	1.090	.131	6.25×10^{-4}	9732.3	153.5	.643	615.6
58D-2	.625	650.3	1.090	.132	6.55×10^{-4}	9096.6	154.5	.622	649.7
68D-1	.656	605.2	1.090	.122	6.65×10^{-4}	7932.7	142.7	.652	604.2
69D-1	.642	579.6	1.082	.117	6.70×10^{-4}	6979.2	136.2	.641	580.0
75D-1	.652	656.7	1.097	.137	6.35×10^{-4}	10621.9	160.6	.648	655.8
75D-2	.702	687.9	1.097	.137	6.65×10^{-4}	10912.6	160.6	.695	685.1
75D-3	.641	685.3	1.097	.137	6.60×10^{-4}	10123.4	161.2	.637	684.1
76D-1	.645	611.5	1.086	.122	6.75×10^{-4}	7637.7	142.8	.643	611.5
77D-1	.654	587.1	1.084	.119	6.65×10^{-4}	7481.1	139.5	.651	586.7
85D-1	.635	665.1	1.092	.130	6.85×10^{-4}	8492.5	152.4	.632	664.4
87D-1	.639	642.1	1.094	.131	6.55×10^{-4}	9094.9	153.3	.637	642.3
89D-1	.678	692.0	1.091	.130	7.03×10^{-4}	9006.7	152.4	.675	691.1
91D-1	.666	568.6	1.083	.116	6.55×10^{-4}	7413.3	135.5	.664	568.4
97D-1	.641	596.6	1.090	.125	6.30×10^{-4}	8768.1	146.3	.638	596.9
98D-1	.633	619.7	1.089	.125	6.55×10^{-4}	8311.8	146.3	.630	619.1
99D-1	.644	546.7	1.084	.116	6.25×10^{-4}	7600.9	136.1	.641	546.2
99D-2	.662	598.7	1.084	.117	6.80×10^{-4}	7265.9	136.9	.659	598.0
6E-1	.731	384.0	1.060	.085	6.30×10^{-4}	4284.7	99.0	.728	384.0
10E-2	.822	295.2	1.045	.066	6.40×10^{-4}	2735.6	76.0	.821	295.3
11E-1	.899	270.7	1.041	.062	6.30×10^{-4}	2642.4	71.1	.894	270.3
14E-1	.861	235.2	1.065	.095	4.91×10^{-4}	5637.9	109.7	.858	235.0

TABLE 2 (cont)

RUN	C_D	Re	M_1	M_R	d ft	α ft/sec^2	U_R ft/sec	$\overline{C}_D$	Re_2
24E-1	.879	291.1	1.079	.112	5.37×10^{-4}	7221.1	131.4	.876	290.8
25E-1	.842	277.4	1.083	.118	4.94×10^{-4}	8166.7	137.7	.838	277.1
27E-1	.842	253.6	1.079	.113	4.69×10^{-4}	7935.6	131.9	.836	252.8
34E-1	.794	305.9	1.089	.128	5.24×10^{-4}	8215.9	149.5	.790	305.6
35E-1	.863	282.6	1.090	.126	4.94×10^{-4}	9200.9	147.9	.859	282.5
49E-1	.847	277.1	1.082	.116	5.04×10^{-4}	7707.3	135.3	.843	276.8
50E-1	.792	298.8	1.088	.123	5.17×10^{-4}	7869.3	143.2	.789	298.6
51E-1	.875	280.9	1.090	.125	4.89×10^{-4}	9279.8	145.6	.873	281.3
52E-1	.795	296.1	1.093	.130	4.99×10^{-4}	8933.1	152.1	.792	296.0
53E-1	.811	278.5	1.095	.131	4.69×10^{-4}	9823.4	153.6	.808	278.4
53E-2	.804	291.9	1.095	.132	4.89×10^{-4}	9420.3	154.3	.800	291.7
55E-1	.899	270.7	1.076	.110	5.04×10^{-4}	7592.3	128.5	.898	270.9
58E-1	.816	273.6	1.079	.114	4.96×10^{-4}	7440.3	133.1	.813	273.6
60E-1	.921	268.8	1.081	.114	4.99×10^{-4}	8151.4	132.7	.916	268.6
62E-1	.841	279.5	1.085	.121	4.99×10^{-4}	8250.8	140.9	.837	279.2
74E-1	.880	280.7	1.089	.124	5.01×10^{-4}	8876.3	145.1	.876	280.7
77E-1	.857	273.8	1.091	.129	4.69×10^{-4}	10105.4	150.9	.852	273.5
78E-1	.836	279.6	1.093	.129	4.81×10^{-4}	9536.3	151.4	.832	279.5
80E-1	.789	295.9	1.097	.133	4.99×10^{-4}	9140.3	155.9	.787	296.1
81E-1	.790	299.8	1.096	.135	4.96×10^{-4}	9520.3	158.6	.785	299.0
93E-1	.677	523.2	1.098	.135	6.10×10^{-4}	9493.6	159.3	.674	523.0
94E-1	.676	563.8	1.097	.135	6.35×10^{-4}	9360.4	158.5	.672	562.6
94E-2	.670	553.2	1.097	.135	6.22×10^{-4}	9488.0	158.7	.667	552.8
99E-1	.726	486.1	1.094	.131	6.42×10^{-4}	8289.5	154.7	.724	486.0
4G-1	.652	536.6	1.092	.132	6.50×10^{-4}	8006.1	155.1	.650	536.4
6G-1	.675	551.3	1.099	.139	6.58×10^{-4}	8781.6	163.1	.672	550.8
6G-2	.683	553.4	1.099	.139	6.60×10^{-4}	8856.6	163.1	.680	552.5
6G-3	.728	549.6	1.099	.138	6.60×10^{-4}	9303.0	162.0	.724	549.1

TABLE 2 (cont)

RUN	C_D	Re	M_1	M_R	d ft	α ft/sec^2	U_R ft/sec	$\overline{C}_D$	Re_2
12G-1	.658	525.9	1.089	.127	6.40×10^{-4}	7875.4	149.5	.656	525.8
12G-2	.691	537.7	1.089	.127	6.55×10^{-4}	8059.2	149.3	.688	537.3
14G-1	.718	515.4	1.085	.121	6.35×10^{-4}	7950.0	140.5	.714	514.4
15G-1	.717	566.5	1.088	.125	6.98×10^{-4}	7525.0	146.3	.715	566.5
15G-2	.734	529.3	1.088	.125	6.55×10^{-4}	8132.8	145.6	.731	528.9
16G-1	.685	553.9	1.089	.126	7.21×10^{-4}	6607.7	146.5	.687	553.3
23G-1	.619	605.3	1.102	.143	6.60×10^{-4}	8957.8	167.3	.615	604.0
23G-2	.642	645.0	1.102	.143	7.01×10^{-4}	8831.8	167.9	.638	643.6
26G-1	.651	512.9	1.092	.132	6.63×10^{-4}	7294.1	154.8	.648	512.8
31G-1	.642	573.1	1.106	.147	6.55×10^{-4}	9222.0	172.8	.639	572.8
33G-1	.667	609.6	1.105	.147	6.98×10^{-4}	8958.0	172.6	.664	609.3
37G-1	.713	576.9	1.101	.143	6.75×10^{-4}	9350.0	166.9	.710	576.4
37G-2	.673	551.2	1.101	.143	6.45×10^{-4}	9242.0	167.0	.670	551.0
43G-1	.946	200.3	1.055	.081	4.69×10^{-4}	4899.0	93.2	.942	200.1
56G-1	.742	413.8	1.059	.088	6.55×10^{-4}	4439.2	101.5	.739	413.5
66G-1	.752	412.3	1.063	.091	6.30×10^{-4}	5060.0	105.4	.750	412.2
72G-1	.710	449.1	1.065	.094	6.60×10^{-4}	4925.4	109.5	.707	448.7
72G-2	.735	421.4	1.065	.093	6.25×10^{-4}	5295.3	108.6	.732	421.3
72G-3	.741	463.0	1.065	.094	6.80×10^{-4}	4993.2	109.6	.738	462.5
72G-4	.730	451.3	1.065	.094	6.65×10^{-4}	5002.1	109.2	.727	450.9
72G-5	.758	436.7	1.065	.094	6.45×10^{-4}	5334.2	109.0	.752	435.0
77G-1	.689	418.5	1.063	.089	6.50×10^{-4}	4347.2	103.7	.689	418.9
79G-1	.697	419.6	1.064	.091	6.40×10^{-4}	4613.8	105.4	.694	419.5
81G-1	.709	394.2	1.059	.087	6.35×10^{-4}	4238.2	100.1	.706	393.8
81G-2	.720	377.5	1.059	.086	6.10×10^{-4}	4453.8	99.8	.716	377.1
84G-1	.715	500.7	1.069	.100	6.85×10^{-4}	5445.0	116.5	.712	500.4
87G-2	.729	494.0	1.074	.104	6.50×10^{-4}	6373.6	121.4	.725	493.8
92G-1	.685	496.7	1.073	.105	6.55×10^{-4}	5969.3	121.9	.682	496.5

TABLE 3

DATA SUMMARY - GLASS BEADS
$.15 < M_R < .30$

RUN	C_D	Re	M_1	M_R	d ft	α ft/sec^2	U_R ft/sec
127-1	.728	787.9	1.179	.239	6.70×10^{-4}	23793.7	287.5
123-1	.591	894.7	1.208	.270	6.65×10^{-4}	25814.3	328.3
135-1	.614	811.5	1.199	.258	6.20×10^{-4}	26337.3	311.9
130-1	.781	689.8	1.168	.225	6.30×10^{-4}	23590.2	269.9
126-1	.681	869.8	1.194	.255	6.80×10^{-4}	25725.8	307.9
154-1	.921	560.4	1.167	.216	5.29×10^{-4}	30660.3	258.5
158-1	.572	707.6	1.177	.241	6.10×10^{-4}	20499.7	289.9
164-1	.701	564.2	1.155	.213	6.30×10^{-4}	16345.1	254.9
165-1	.857	629.8	1.163	.223	6.35×10^{-4}	23180.4	268.2
166-1	.857	615.0	1.157	.214	6.55×10^{-4}	20300.4	256.9
167-1	.639	778.9	1.197	.258	6.20×10^{-4}	26551.7	312.8
169-1	.656	751.4	1.181	.244	6.35×10^{-4}	23458.8	294.9
203-2	.653	1378	1.130	.180	9.58×10^{-4}	13173.6	212.8
204-2	.686	1290	1.120	.166	9.83×10^{-4}	11265.9	195.8
205-2	.652	1577	1.138	.188	1.04×10^{-3}	13456.0	222.9
225-1	.705	1269	1.126	.173	9.42×10^{-4}	13130.3	205.0
226-1	.584	1331	1.135	.185	9.12×10^{-4}	13132.2	220.3
231-1	.594	1304	1.123	.170	9.88×10^{-4}	10177.5	201.9
232-1	.736	1150	1.105	.150	1.01×10^{-3}	9242.1	177.7
238-1	.638	1239	1.121	.167	9.63×10^{-4}	10803.2	199.0
242-1	.719	1351	1.128	.175	9.88×10^{-4}	13196.3	208.2
244-1	.712	1214	1.110	.159	1.00×10^{-4}	10089.5	187.4
247-1	.655	1158	1.118	.163	9.27×10^{-4}	10735.1	192.5
250-1	.631	1296	1.134	.184	8.97×10^{-4}	14163.7	219.2
283-1	.788	803.1	1.150	.209	9.22×10^{-4}	11821.9	248.9
284-1	.834	608.8	1.119	.170	8.92×10^{-4}	8071.0	200.9
286-1	.739	783.0	1.147	.206	9.17×10^{-4}	10736.5	244.9
290-1	.524	896.9	1.163	.230	9.17×10^{-4}	9822.3	274.5
300-1	.766	571.5	1.142	.187	6.56×10^{-4}	14508.9	223.1
300-2	.838	566.6	1.142	.185	6.56×10^{-4}	15594.7	221.2
301-1	.585	866.2	1.207	.258	6.67×10^{-4}	23411.8	312.7
301-3	.571	853.7	1.207	.258	6.56×10^{-4}	23317.1	313.2
302-1	.889	656.8	1.161	.208	6.56×10^{-4}	21737.3	249.4
304-1	.629	804.1	1.193	.246	6.56×10^{-4}	22704.7	296.8
304-2	.657	774.6	1.194	.244	6.37×10^{-4}	24082.6	294.6

TABLE 4

DATA SUMMARY - WINCHESTER WESTERN HP 295 BALL POWDER

RUN	C_D	Re	M_1	M_R	d ft	α ft/sec^2	U_R ft/sec
389-1	.939	596.9	1.101	.121	6.56×10^{-4}	11678.3	142.6
390-1	.969	603.1	1.100	.122	6.56×10^{-4}	12299.6	144.1
390-2	1.004	595.3	1.100	.124	6.56×10^{-4}	12426.3	142.3
391-1	.927	614.5	1.101	.124	6.56×10^{-4}	12227.2	146.8
577-1	.685	662.6	1.071	.099	9.32×10^{-4}	5681.3	116.5
577-2	.758	716.7	1.071	.099	1.01×10^{-3}	5771.7	116.2
578-1	.784	692.4	1.068	.096	1.02×10^{-3}	5499.8	112.1
578-2	.691	752.7	1.068	.097	1.09×10^{-3}	4618.3	113.5
581-1	.783	665.3	1.067	.094	9.92×10^{-4}	5472.3	110.8
587-1	.690	683.4	1.068	.094	1.03×10^{-3}	4596.2	110.0
591-1	.919	689.0	1.069	.096	9.78×10^{-4}	6832.7	112.1
593-1	.774	668.8	1.068	.095	9.73×10^{-4}	5557.4	110.1
596-1	.655	744.3	1.068	.097	1.05×10^{-3}	4591.2	113.2
607-2	.677	734.4	1.070	.097	1.03×10^{-3}	4831.5	112.0
610-1	.701	724.0	1.070	.098	1.00×10^{-3}	5280.0	113.6
612-1	.777	688.2	1.069	.098	9.57×10^{-4}	6060.1	113.2
613-1	.530	737.7	1.069	.100	1.00×10^{-3}	4160.1	116.1
614-1	.692	722.8	1.069	.098	1.00×10^{-3}	5218.2	113.8

TABLE 5

DATA SUMMARY - SAPPHIRE BALLS*

RUN	C_D	Re	M_1	M_R	α ft/sec^2	U_R ft/sec
701-1	.581	1477	1.101	.149	3445.3	174.1
720-1	.530	1462	1.100	.146	3048.7	170.8
723-1	.548	1479	1.100	.148	3229.0	172.9
725-1	.572	1474	1.099	.148	3369.9	173.0
726-1	.556	1487	1.101	.149	3334.6	174.4
728-1	.561	1467	1.099	.147	3294.2	173.0
728-2	.571	1468	1.099	.147	3356.4	173.0
735-1	.624	855.9	1.099	.149	2181.2	175.3
740-1	.473	956.0	1.107	.160	1958.2	187.8
741-1	.533	968.8	1.108	.162	2259.9	189.9
743-1	.521	955.2	1.107	.160	2160.1	188.0
746-1	.546	949.4	1.108	.161	2266.0	189.0
751-1	.465	1178	1.183	.257	4016.1	307.5
756-1	.521	933.3	1.104	.156	2048.6	183.0
756-2	.531	932.9	1.104	.156	2083.8	182.9
758-1	.525	923.3	1.103	.154	2010.0	180.6
761-1	.534	920.8	1.102	.154	2035.0	184.0
767-1	.501	1068	1.138	.202	2988.7	238.8
767-2	.525	1069	1.138	.202	3134.0	238.9
775-1	.522	1036	1.135	.193	2887.4	228.5
776-1	.484	1116	1.151	.217	3268.1	257.6
777-1	.520	1088	1.140	.205	3209.1	242.5
778-1	.492	1106	1.147	.213	3213.3	252.2
779-1	.520	1083	1.138	.202	3132.5	238.4
781-1	.549	1061	1.136	.200	3199.2	235.8
783-1	.585	1038	1.135	.198	3313.1	233.9
820-1	.488	1181	1.175	.250	4061.5	297.8
821-1	.527	1158	1.177	.250	4301.4	297.5
828-1	.506	1224	1.196	.276	4895.5	330.5
833-1	.492	1234	1.227	.313	5590.5	379.6

*Diameter, d, is always 1.3021×10^{-3} ft for sapphire balls.

REFERENCES

1. "Dynamics of Two-Phase Flow In Rocket Nozzles," Fourth Quarterly Technical Progress Report, 26 May 1962, United Technology Corporation, Contract No. NOW-61-0760-C.

2. Ingebo, R.D., "Drag Coefficients for Droplets and Solid Spheres in Clouds Accelerating in Air Streams," NACA TN 3762, 1956.

3. Hanson, A.R., "The Effects of Relative Velocity on Evaporation of a Liquid Fuel Spray," University of Michigan, Ph.D. Thesis, 1951.

4. Bolt, J.A. and Wolf, L.W., "Drag Coefficients for Burning Kerosene Drops," University of Michigan ERI Project No. 2253: 3-6-P, 1954.

5. Rabin, E., Schallenmuller, A.R., and Lawhead, R.B., "Displacement and Shattering of Propellent Droplets," Rocketdyne, AFOSR-TR-60-75, 1960.

6. Rudinger, G., "Experiments on Shock Relaxation in Particle Suspensions in a Gas and Preliminary Determination of Particle Drag Coefficients," Cornell Aeronautical Laboratory, Project Squid Tech. Report CAL-90-P, July 1963.

7. Torobin, L.B. and Gauvin, W.H., "Introductory Concepts and Idealized Sphere Motion in Viscous Regime," The Canadian Journal of Chemical Engineering, 37:129, 1959.

8. Torobin, L.B. and Gauvin, W.H., "The Sphere Wake in Steady Laminar Fluids," The Canadian Journal of Chemical Engineering, 37:157, 1959.

9. Torobin, L.B. and Gauvin, W.H., "Accelerated Motion of a Particle in a Fluid," The Canadian Journal of Chemical Engineering, 37:224, 1959.

10. Torobin, L.B. and Gauvin, W.H., "The Effects of Particle Rotation, Roughness, and Shape," The Canadian Journal of Chemical Engineering, 38:142, 1960.

REFERENCES (cont)

11. Torobin, L. B. and Gauvin, W. H., "The Effects of Fluid Turbulence on the Particle Drag Coefficient," The Canadian Journal of Chemical Engineering, 38:189, 1960.

12. Torobin, L. B. and Gauvin, W. H., "The Drag Coefficients of Single Spheres Moving in Steady and Accelerated Motion in a Turbulent Fluid," Pulp and Paper Institute of Canada and Department of Chemical Engineering, McGill University, Tech. Report No. 193, 1960.

13. Crowe, C. T., "Drag Coefficients of Inert, Burning, or Evaporating Particles Accelerating in Gas Streams," University of Michigan, Ph.D. Thesis, 1961.

14. "Fundamentals of Gas Dynamics," H.W. Emmons, Ed., High Speed Aerodynamics and Jet Propulsion, Vol. 3, Princeton University Press, 1958.

15. Emrich, R. J. and Curtis, C. W., "Attenuation in the Shock Tube," Journal of Applied Physics, Vol. 24, No. 3, 1953.

16. Hilsenrath, J., Beckett, C. W., et al., Tables of Thermal Properties of Gases, National Bureau of Standards Circular 564, 1955.

17. Beers, Y., Introduction to the Theory of Error, Addison-Wesley Publishing Company, 1957.

18. Schlichting, H., Boundary Layer Theory, Trans. by J. Kestin, McGraw-Hill Book Co., Inc., 1960.

19. Moore, F. K., "Aerodynamic Effects of Boundary Layer Unsteadiness," Sixth Anglo-American Aeronautical Conference, 1957.

20. Rosenhead, L., Laminar Boundary Layers, Oxford Press, 1963.

21. Sarpkaya, T., "Separated Flow About Lifting Bodies and Impulsive Flow About Cylinders," Paper presented at the Second Annual AIAA Meeting, AIAA Paper No. 65-396, 1965.

REFERENCES (cont)

22. Maccoll, J.W., Journal of the Royal Aeronautical Society, 32:777, 1928.

23. Davies, J.M., Journal of Applied Physics, 20:821, 1949.

24. Pasternak, I.S., Ph.D. Thesis, McGill University, 1959.

25. Luthander, S. and Rydberg, A., Physik. Z., 36:552, 1935.

26. Garstang, T.E., Proceedings of the Royal Society, 142A;491, 1933.

27. Drazin, M.P., Proceeding of the Cambridge Philosophical Society, 47:142, 1951.

28. Keim, S.R., "Fluid Resistance to Cylinders in Accelerated Motion," Proceedings of the American Society of Civil Engineers, 82:HY6, (J. Hr. Div.), Paper 1113, 1956.

29. Bugliarello, G., "La Resistenza al Moto Accelerato di Sfere in Acqua," La Richerca Scientifica, 26:437, 1956.

30. Hoerner, S., "Tests of Spheres with Reference to Reynolds Number, Turbulence, and Surface Roughness," Luftfahrtforschung, Vol. 12, No. 1, 1935.

31. Lunnon, R.G., "Fluid Resistance to Moving Spheres," Proceedings of the Royal Society, Series A., Vol. 110, 1926.

32. Carlson, D.J. and Hoglund, R.F., "Particle Drag and Heat Transfer in Rocket Nozzles," AIAA Journal, Vol. 2, No. 11, 1964.

33. Iversen, H.W. and Balent, R., "A Correlating Modulus for Fluid Resistance in Accelerated Motion," Journal of Applied Physics, Vol. 22, No. 3, 1951.

34. Hoglund, R.F., "Recent Advances in Gas Particle Nozzle Flows," American Rocket Society Solid Propellent Rocket Conference, Baylor University, 1962.

REFERENCES (cont)

35. Gilbert, M., Davies, L., and Altman, D., "Velocity Lag of Particles in Linearly Accelerated Combustion Gases," Jet Propulsion, Vol. 25 1955.

36. Liepmann, H.W. and Roshko, A., Elements of Gas Dynamics, John Wiley and Sons, Inc., 1957.

37. Spokes, G.N., "The Role of Aluminum and its Oxides as Sources or Moderators of Electrons in Aluminized Solid Propellent Rocket Exhausts," Final Report, Part 2, August 1964, Stanford Research Institutes Contract No. AF 04(694)-128.

38. Dryden, H.L., "Review of Published Data on the Effect of Roughness on Transition from Laminar to Turbulent Flow," Journal of the Aeronautical Sciences, Vol. 20, No. 7, pp. 477-482, July 1953.

39. Klebanoff, P.S., Schubauer, G.B., and Tidstrom, K.D., "Measurements of the Effect of Two-Dimensional and Three Dimensional Roughness Elements on Boundary Layer Transition," Journal of the Aeronautical Sciences, Vol. 22, No. 11, pp. 803-804, Nov. 1955.

40. Smith, A.M.O. and Clutter, D.W., "The Smallest Height of Roughness Capable of Affecting Boundary-Layer Transition," Journal of the Aeronautical Sciences, Vol. 26, No. 4, pp. 229-245, April 1959.

41. Potter, J.A. and Whitfield, J.D., "Effects of Unit Reynolds Number, Nose Bluntness, and Roughness on Boundary Layer Transition," AEDC-TR-60-5, March 1960.

NASA-Langley, 1966 CR-418